Tuning *g* factors of core-shell nanoparticles by controlled positioning of magnetic impurities

G. D. Sanders,[1] J. L. Musfeldt,[2] and C. J. Stanton[1]
[1]*Department of Physics, University of Florida, Gainesville, Florida 32611-8440, USA*
[2]*Department of Chemistry, University of Tennessee, Knoxville, Tennessee 37996, USA*
(Received 20 October 2015; revised manuscript received 3 February 2016; published 23 February 2016)

We present a theoretical platform for modeling the electronic and magneto-optic properties of magnetically doped core-shell nanoparticles that has, as a central prediction, a mechanism by which the *g* factors in these nanoparticles can be tuned over a wide range by controlled positioning of magnetic impurities. We illustrate this effect for wide-gap Mn-doped CdS-ZnS core-shell particles and point out several unexpected trends that merit extended experimental investigation. The ability to tune *g* factors will make core-shell nanostructures viable candidates for spintronic applications, and the comprehensive modeling approach outlined here will be a powerful tool for predicting their properties as well as for optimizing the design of novel spintronic devices.

DOI: 10.1103/PhysRevB.93.075431

I. INTRODUCTION

Doping by conventional nonmagnetic impurities allows for control of carriers in semiconductors and is the basis for most conventional semiconductor devices [1,2]. Magnetic impurities, on the other hand, bring additional functionality. Besides acting as isolated paramagnetic centers, the exchange interaction between localized magnetic impurity *d* electrons and the itinerant host electrons and holes results in tunable magneto-optical properties that can be exploited in spintronic applications. Here, the carrier spin degree of freedom (rather than charge) is used in device operations [3–5], and the spin of the electron or hole can be controlled by external stimuli such as magnetic, electric [6], and optical fields [7,8]. The design and optimization of carrier spin polarization is thus an important goal. This motivates the sustained interest in III-V and II-VI dilute magnetic semiconductors which incorporate magnetic impurities, such as manganese, to modify the electronic, magnetic, and magneto-optical properties [9–13].

It is well known that careful control of magnetic impurities in dilute magnetic semiconductor thin film heterostructures provides great flexibility for engineering magnetic *g* factors and magneto-optical properties. Recently *g* factors have been studied in ferromagnetic InMnAs and InMnAs at high magnetic fields with Curie temperatures above 300 K [14]. It was therefore anticipated that precise control of magnetic impurity doping in core-shell nanoparticles and other nanoscale heterostructures could lead to new functionalities [15–21]. Chemists now have the ability to selectively dope core-shell nanoparticles with magnetic impurities at a specific and precisely defined radius [20,22–24]. For instance, radial position controlled Mn doping of zinc-blende CdS-ZnS core-shell nanoparticles was achieved using a three-step process which includes CdS-core growth, Mn-dopant growth in a thin spherical doping layer (inside either core or shell), and ZnS-shell growth [20,22–24]. As a result, the optical properties of these nanoparticles can be tuned by varying the core and shell thicknesses and the spintronic properties can be tailored by precise positioning of the magnetic impurities. In addition to providing for control of carrier concentration and spin, dopants themselves can also serve as sensitive radial pressure gauges for measuring lattice strains due to lattice mismatch at the core-shell interface [25]. In this paper, we discuss radial position controlled magnetic impurity doping in type I core-shell nanoparticles in which both electrons and holes are confined in the core by barrier potentials in the shell. An additional benefit of the semiconductor shell is that it provides a barrier between the optically active core and the environment. The active core region is thus less sensitive to surface chemistry and photo-oxidation and provides for efficient passivation of surface states. This is useful for chemical sensing, biological sensing, and solar cells [26–32] and is also advantageous for preserving spin polarization.

Motivated by breakthroughs in the growth of controllably doped core-shell nanoparticles and the ongoing exploration of their properties [20,22–24], we developed a theoretical model to describe the electronic states, magnetic *g* factors, and magneto-optical properties in systems with radial position controlled magnetic impurity doping. In addition to providing the foundational understanding of excitation processes, we examine the role of strain and ultrahigh magnetic fields. While we focus on the large-gap CdS-ZnS system with Mn doping in an effort to compare with emerging experimental work [20,22–24], the comprehensive modeling approach outlined here can easily be extended to new materials and will be a powerful predictor of similar effects in other candidate systems.

II. MODELING AND METHODS

Our theoretical approach is based on the effective mass formalism. It has been used extensively to study spherical semiconductor nanoparticles (for instance, zinc-blende [33] and wurtzite [34] materials) as well as various core-shell systems [35–38]. Existing implementations do not, however, include magnetic impurity dopants. In this work, we reach beyond traditional effective mass models to include the effects of strain and position dependent doping by magnetic impurities in core-shell nanoparticles placed in a static magnetic field. Specifically, we consider CdS-ZnS core-shell quantum dots doped by magnetic Mn^{2+} impurities implanted at a preselected radius, R_i, in an infinitesimally thin spherical doping layer. A schematic diagram is shown in Fig. 1. The nanoparticle consists of an inner CdS core of radius R_c surrounded

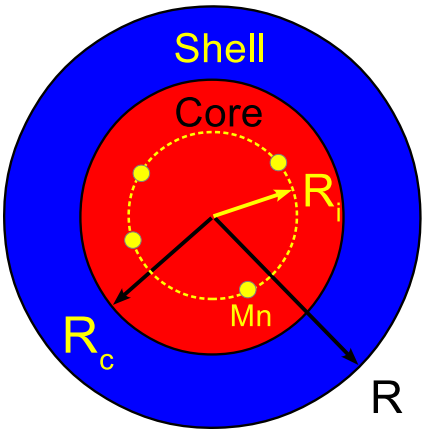

FIG. 1. Schematic diagram of Mn-doped spherical core-shell nanoparticle with an outer shell radius R and an inner core radius R_c. The core-shell nanoparticle is doped with magnetic Mn impurities in an infinitely thin shell (yellow dashed line) located at radius R_i. In general the Mn impurities can be embedded in either the core or shell regions.

by a ZnS shell with outer radius R. The nanoparticle is doped with radial position controlled magnetic Mn impurities. The Mn impurities are all located in an infinitesimally thin shell at radius R_i as shown in the figure. The Mn impurity doping shell in Fig. 1 is shown embedded in the inner core but could equally well be embedded in the outer shell. A static magnetic field is applied which defines the z direction.

Our model allows for different effective mass parameters in core and shell as well as s-d and p-d exchange interactions between itinerant carriers and localized Mn d electrons. Due to the wide band gaps in CdS and ZnS, the conduction and valence band effective mass Hamiltonians are decoupled. The strain in the core-shell nanoparticle arises from the lattice mismatch between core and shell regions and is assumed to be pseudomorphic and the effect of this strain field on the electronic states is included in the Bir-Pikus formalism [39]. For simplicity, the Mn impurities are treated in a *virtual crystal* and *mean field* approximation [40,41] in which the impurities are smeared out over the surface of an infinitesimally thin spherical Mn doping layer. We assume an sp-d exchange interaction between the localized Mn^{2+} d electrons and the delocalized conduction s and valence p electrons. We assume by default that the core-shell nanoparticle is paramagnetic. Ferromagnetic core-shell nanoparticles (should they exist) could also be studied in the mean field approximation taking the Curie temperature as an input parameter. In addition, the elastic properties of CdS and ZnS are assumed to be isotropic and characterized by a Young's modulus and Poisson's ratio. These assumptions neglect orientation effects in the crystal structure thus maintaining spherical symmetry.

External magnetic fields in the effective mass theory are introduced through standard Peierls substitution in the wave vector and the addition of the Zeeman energy [42,43]. The Peierls substitution is widely used to treat homogeneous magnetic field effects in the effective mass theory of semiconductor heterostructures [44–49].

It is known that as the size of a nanostructure decreases, the effective mass model begins to break down [50–54]. In applying the effective mass model to CdS-ZnS core-shell nanoparticles, we need to have some idea of the size range for which it is valid. The size dependence of electronic properties of CdS and ZnS crystallites has been studied both theoretically and experimentally [52,53]. Experimentally, these crystallites exhibit the same zinc-blende structure and lattice constant as the bulk material [52]. Lippens and Lanoo in Ref. [52] study the band gap of small CdS and ZnS crystallites theoretically using the effective mass approximation and a tight binding method. In Fig. 4 of Ref. [52] the computed band gap for ZnS quantum dots in the effective mass approximation is compared with the results of a tight binding model. The two calculations converge for ZnS diameters greater than 100 Å. In Fig. 5 of Ref. [52] experimental CdS crystallite band gaps are shown as a function of diameter and compared with effective mass and tight binding calculations. It is found that theory and experiment agree for CdS diameters greater than 60 Å. CdS clusters have also been studied experimentally in Ref. [53] where the validity of the effective mass approximation is investigated. In Fig. 2 of Ref. [53] we see that the effective mass approximation begins to break down for CdS cluster sizes below about 60 Å. We therefore expect that our effective mass model can be applied to CdS-ZnS core-shell nanoparticles with diameters down to about 100 Å or $R \gtrsim 50$ Å.

Our analysis does not include Coulomb effects. The interested reader is referred to Ref. [55] for additional discussion of impurity states in semiconductor nanocrystals including Coulomb and confinement effects in externally applied fields. Details of our effective mass formalism can be found in the Appendix.

III. RESULTS AND DISCUSSION

To illustrate our effective mass theory, we calculate room temperature electronic states, magnetic g factors, and magneto-optical properties in CdS-ZnS spherical core-shell nanoparticles of radius R having an inner CdS core with radius $R_c = R/2$ embedded in a ZnS shell with inner radius R_c and outer radius R. The structure of the nanoparticles is shown schematically in Fig. 1. We consider two such nanoparticles with $R = 50$ Å and $R = 100$ Å since these structures are typical of Mn radial position doped core-shell nanoparticles that have been grown experimentally [20,22–24]. We refer to these two structures as the 100 Å diameter and 200 Å diameter core-shell nanoparticle, respectively.

A. Undoped CdS-ZnS nanoparticles

As a prelude to examining the effect of Mn doping on magneto-optical properties, we first calculate room temperature magneto-optical properties in CdS-ZnS spherical core-shell nanoparticles in the absence of magnetic impurities.

The band edge of the nanoparticle as a function of radius is shown in Fig. 2. The CdS core has a band gap of 2.5 eV while the ZnS shell has a 3.54 eV band gap. The band gap mismatch is thus $\Delta E_g = 1.04$ eV. Energies are measured relative to the top of the CdS valence band edge. The conduction band gap offset is taken to be $Q_c = 0.6$ meaning that 60% of

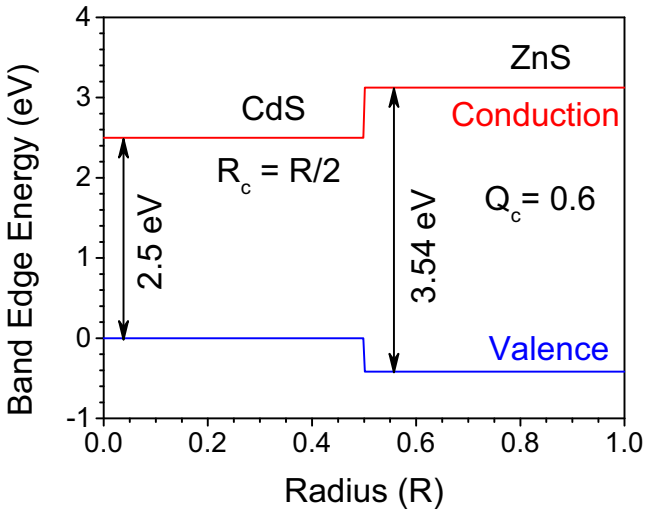

FIG. 2. Band edge in a CdS-ZnS spherical core-shell quantum dot of radius R with r plotted in units of R. The nanoparticle consists of a CdS core with radius $R_c = R/2$ surrounded by a ZnS shell. The conduction band offset is $Q_c = 0.6$.

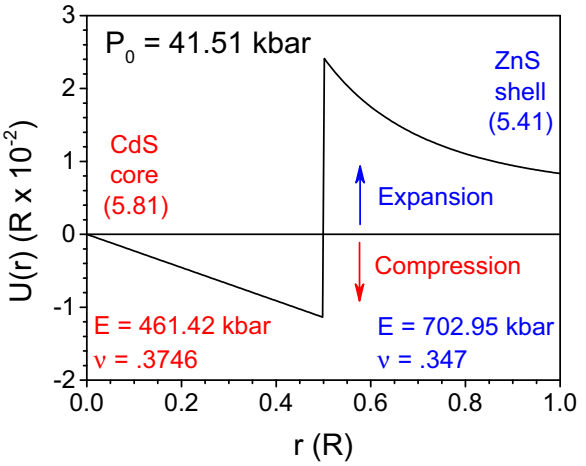

FIG. 3. Radial displacement field $U(r)$ due to strain as a function of r in CdS-ZnS core-shell nanoparticles where r and $U(r)$ are plotted in units of the nanoparticle radius R. The CdS core radius is $R_c = R/2$. Strain is due to lattice mismatch between the CdS core and ZnS shell, whose lattice constants are 5.81 Å and 5.41 Å, respectively. The Young's modulus, E, and Poisson's ratio, ν, in CdS and ZnS are also indicated. The CdS core undergoes compression while the ZnS shell undergoes expansion. The interface contact pressure $P_0 = 41.51$ kbar for all values of R.

the band gap mismatch is accommodated in the conduction band and 40% in the valence band. Our choice of $Q_c = 0.6$ is supported by a study of optical properties in CdS-ZnS core-shell quantum dots reported in Ref. [56]. In this study, the conduction band offset was found to be about twice the valence band offset. We can see from Fig. 2 that the CdS core is a spherical well and the ZnS shell is a barrier. The conduction and valence barrier heights are 0.624 eV and 0.416 eV, respectively.

The lattice mismatch between the CdS core and ZnS shell gives rise to significant strain-induced modifications to the electronic structure. The effect of strain on the electronic structure is described by the Bir-Pikus strain Hamiltonian H_S defined in the Appendix in Eq. (A14). The assumption of homogeneous elastic properties preserves spherical symmetry and simplifies the problem. The Bir-Pikus strain Hamiltonian depends on the displacement field $U(r)$ determined by elastic continuum theory [57]. The displacement field $U(r)$ in the core and shell, $U_c(r)$ and $U_s(r)$, are defined in the Appendix in Eqs. (A21) and (A22). The displacement field $U(r)$ is shown in Fig. 3 as a function of r for core-shell nanoparticles with a core radius $R_c = R/2$. Note that the radius r and displacement field $U(r)$ in Fig. 3 are plotted in units of the nanoparticle radius R and $R \times 10^{-2}$, respectively. The CdS core has a larger lattice constant ($a_0 = 5.81$ Å) than the ZnS shell ($a_0 = 5.41$ Å). As a result, the core undergoes compression while the shell undergoes expansion. There is a discontinuity in the displacement field at the core-shell interface due to the shrink-fit boundary condition defined in Eq. (A23) which is used to determine the contact pressure at the core-shell interface. The interface contact pressure in all nanoparticles with $R_c = R/2$ is $P_0 = 41.51$ kbar independently of R. This is easily seen from Eq. (A21) in the Appendix. The interface contact pressure is given by

$$P_0 = -\frac{U_c(R_c)}{R_c}\,\frac{E_c}{1-2\nu_c}, \tag{1}$$

where $U_c(R_c)/R = -1.128 \times 10^{-2}$ and $R_c/R = 0.5$ can be read off directly from Fig. 3 and $E_c = 461.42$ kbar and $\nu_c = 0.3746$ are the Young's modulus and Poisson's ratio in the CdS core.

In our calculations, the electronic states are given by the expansion in Eq. (A31). The basis states are the particle in spherical box eigenstates $|n,l,m\rangle$ given in Eq. (A32) for a spherical box with radius R and an infinite barrier. We keep terms in the electronic state expansion up to $N = 6$ for a total of 91 (n,l,m) basis states. To determine when convergence is achieved, we vary N until the energy levels change by a small amount when N is increased further. To verify that $N = 6$ is sufficient for convergence, we tried $N = 7$ increasing the number of (n,l,m) basis states from 91 to 140. For the 100 Å diameter quantum dot increasing N from 6 to 7 shifts the ground state electron and hole energies at $B = 0$ by 0.8 meV and 0.56 meV, respectively. For the 200 Å diameter quantum dot the corresponding electron and hole energy shifts are 0.1 meV and 0.2 meV.

In narrow-gap semiconductors coupling between electron and hole levels can be significant. In general the conduction band states are six component spinors with two electron and six hole components. In the wide-gap semiconductors CdS and ZnS the coupling of electron and hole states can be safely neglected. Thus, the conduction band states contain two electron components and the valence band states contain six hole components.

In the absence of a magnetic field, the conduction band ground state is twofold spin degenerate, i.e., pure electron spin-up and spin-down states. The valence band hole states are mixed by off-diagonal components of the effective mass Hamiltonian. The hole ground state is fourfold degenerate consisting of two predominantly heavy-hole (spin-up and

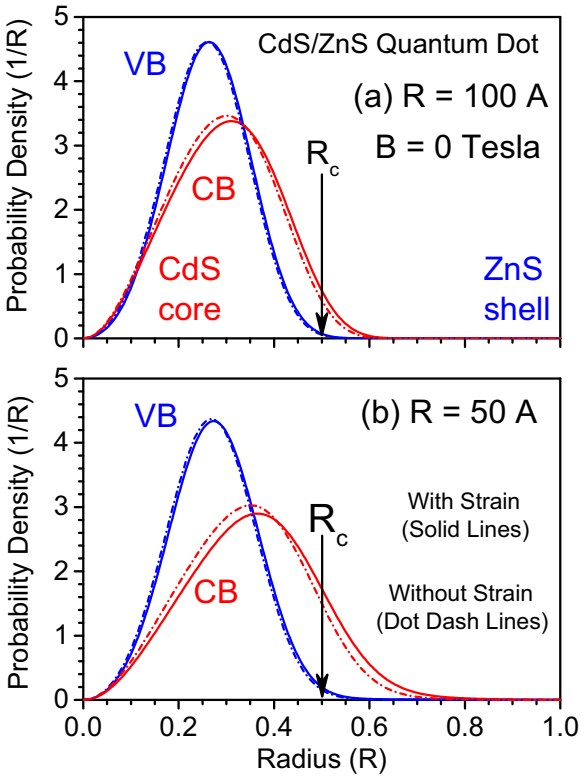

FIG. 4. Normalized radial probability densities as a function of r plotted in units of the nanoparticle radius R in CdS-ZnS spherical core-shell nanoparticles with (a) $R = 100$ Å and (b) $R = 50$ Å. CdS core radii are $R_c = R/2$. Probability densities for twofold-degenerate conduction electron ground states (CB) are shown as red curves and probability densities for fourfold-degenerate valence light-hole and heavy-hole (VB) ground states are shown in blue. Results neglecting strain are dot-dashed lines and results including strain are solid lines.

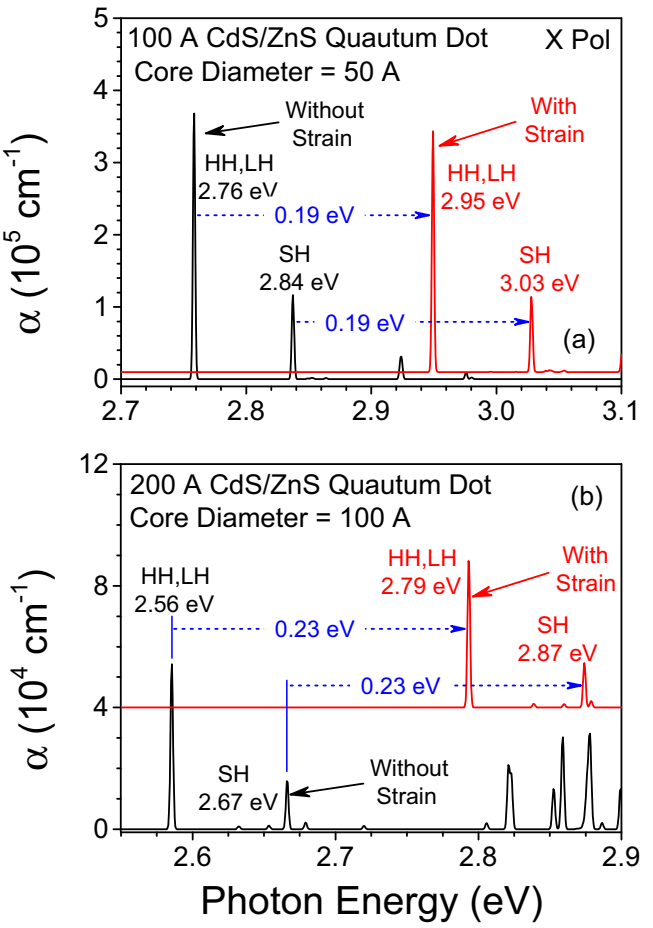

FIG. 5. Absorption coefficient for linearly polarized light in undoped CdS-ZnS core-shell nanoparticles with diameters of (a) 100 Å ($R = 50$ Å) and (b) 200 Å ($R = 100$ Å). The CdS core diameter is always half the nanoparticle diameter ($R_c = R/2$). Absorption coefficients are calculated using Fermi's golden rule with (red) and without (black) inclusion of strain effects. All linewidths are 2 meV. Peaks labeled heavy hole (HH), light hole (LH), and split-off hole (SH) are transitions between the hole and conduction band ground states.

spin-down) states and two predominantly light-hole (spin-up and spin-down) states.

Quantum confinement in core-shell nanoparticles in the absence of a magnetic field is illustrated in Fig. 4. We plot radial probability density for the electron and hole ground states in our 100 Å and 200 Å diameter CdS-ZnS core-shell nanoparticles. The twofold-degenerate conduction electron ground state (CB) is shown in red and the fourfold-degenerate hole ground state (VB) is shown in blue. In the 200 Å diameter nanoparticle [see Fig. 4(a)], the electrons are tightly confined to the CdS core with very little leakage into the ZnS barrier. When the size of the nanoparticle is cut in half [see Fig. 4(b)], the electrons start to tunnel into the ZnS barrier. The holes are more massive than the electrons and are almost completely confined to the CdS core as seen in Fig. 4. The reason the heavy and light holes are degenerate and have the same radial probability densities can be understood from spherical symmetry by noting that the expectation values $\langle p_x^2 \rangle$, $\langle p_y^2 \rangle$, and $\langle p_z^2 \rangle$ are equal in the spherical ground state and hence the expectation value of $Q \propto p_x^2 + p_y^2 - 2\ p_z^2$ in the Landau Hamiltonian [Eq. (A4)] must *vanish*. As a consequence, the heavy-hole and light-hole energy expectation values, proportional to $\langle P + Q \rangle$ and $\langle P - Q \rangle$, are also equal. We thus note that unlike a quantum well structure, the heavy-light hole degeneracy *is not split* in the spherical quantum dot geometry.

The computed absorption coefficient as a function of photon energy for linearly polarized light incident on undoped CdS-ZnS quantum dots is shown in Fig. 5 for our 100 Å and 200 Å diameter core-shell quantum dots. The absorption coefficient is obtained from Fermi's golden rule assuming all transition linewidths are 2 meV. The black curves in Fig. 5 are the computed absorption coefficients neglecting strain effects while the red curves are the computed absorption coefficients *including* strain effects. From Fig. 5, we see that the inclusion of strain has a pronounced effect on the absorption coefficient. The inclusion of pseudomorphic strain shifts the lowest-lying heavy-hole, light-hole, and split-off-hole transitions approximately 0.19 eV to higher energies in the 100 Å diameter nanoparticle and 0.23 eV in the 200 Å nanoparticle while leaving transition oscillator strengths essentially unchanged. The total oscillator strength of the

two degenerate SH transitions are exactly a third of the total oscillator strength of the four degenerate HH and LH transitions. We note that in strained heterostructures, such as biaxially strained quantum wells, the strain lifts the heavy-hole and light-hole degeneracy. In our core-shell spherical nanoparticles, on the other hand, the heavy-hole and light-hole levels remain degenerate in the presence of strain because the expectation value of $Q_\varepsilon \propto \varepsilon_{xx} + \varepsilon_{yy} - 2\,\varepsilon_{zz}$ in the strain Hamiltonian [Eq. (A14)] also vanishes in the spherical ground state. The shift in the lowest-lying transition energies due to strain is the expectation value of $\Delta E_{\text{strain}} \approx a\ \nabla\cdot\boldsymbol{U}(\boldsymbol{r})$ where $a = a_c - a_v$ is the hydrostatic deformation potential and $\boldsymbol{U}(\boldsymbol{r})$ is the strain-induced radial displacement field (shown in Fig. 3). In Fig. 5, strain shifts the transition energies upward because (i) the deformation potentials in the CdS core and ZnS shell are negative and (ii) the CdS core is under compressive strain because of its larger lattice constant so that $\nabla\cdot\boldsymbol{U}(\boldsymbol{r})$ is negative in the region where the carriers primarily reside. Thus $\Delta E_{\text{strain}} > 0$.

With strain effects included, the lowest transition is the HH,LH peak at 2.95 eV in the 100 Å core-shell nanoparticle and 2.79 eV in the 200 Å nanoparticle. These peaks are fourfold degenerate with two dipole-allowed transitions between the heavy-hole and conduction states. The remaining two dipole-allowed transitions are from light-hole states to conduction states. For allowed transitions ($\Delta J_z = \pm 1$), the dipole-allowed heavy-hole transitions ($J = \frac{3}{2}, J_z = \pm\frac{3}{2}$) are (hh ↑ to cb ↑) and (hh ↓ to cb ↓) and the dipole-allowed light-hole transitions ($J = \frac{3}{2}, J_z = \pm\frac{1}{2}$) are (lh ↑ to cb ↓) and (lh ↓ to cb ↑).

The strong dipole-allowed SH transitions in Fig. 5 at 3.03 eV in the 100 Å diameter ($R = 50$ Å) core-shell nanoparticle and 2.87 eV in the 200 Å diameter ($R = 100$ Å) nanoparticle are twofold-degenerate transitions between the lowest split-off hole states ($J = \frac{1}{2}, J_z = \pm\frac{1}{2}$) and the lowest conduction states. The two dipole-allowed transitions are (sh ↑ to cb ↓) and (sh ↓ to cb ↑).

In Fig. 5, the lowest-lying HH,LH transition energies (including strain) in the absence of a magnetic field are 2.95 eV and 2.79 eV in our $R = 50$ Å and $R = 100$ Å nanoparticles with CdS core radius $R_c = R/2$. These transition energies can be tuned by varying the ZnS shell thickness and CdS core radius. Figure 6 shows the photon energy of these HH,LH transitions as a function of CdS core radius with and without the inclusion of strain for two different nanoparticle sizes. Depending on the CdS core radius, the HH,LH transition energy can be varied over a wide range from roughly 2.6 to 3.6 eV. The inclusion of strain always shifts the lowest-lying HH,LH transition to higher energy. Of course at $R_c = R$ there is no shell and hence no strain. Likewise, there is no core and hence no strain for $R_c = 0$. By decreasing R, the transition energy is further increased by enhanced quantum confinement.

When an external magnetic field, B, is applied, the spin-degenerate energy levels are split. Here we only consider 100 Å diameter ($R = 50$ Å) CdS-ZnS core-shell nanoparticles with 50 Å diameter ($R_c = 25$ Å) CdS cores as results for 200 Å diameter ($R = 100$ Å) nanoparticles are somewhat redundant. The energy levels for the two lowest conduction states and the four lowest hole states (two heavy and two light) are shown

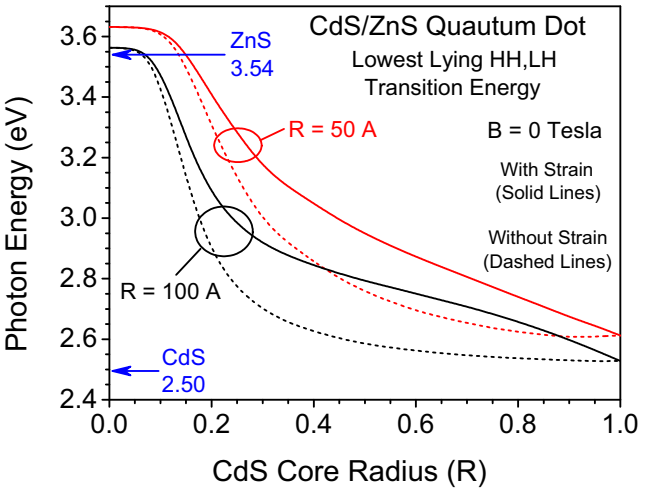

FIG. 6. Photon energies for optical transitions between the fourfold-degenerate heavy-hole (HH) and light-hole (LH) ground states and the twofold-degenerate electron ground state in undoped $R = 100$ Å (black) and $R = 50$ Å (red) CdS-ZnS core-shell quantum dots. The CdS core radius is plotted in units of the nanoparticle radius R. Transition energies, with strain (solid) and without strain (dashed), are plotted as a function of CdS core radius. The direct band gaps for ZnS (3.54 eV) and CdS (2.50 eV) are marked by blue arrows.

in Fig. 7(a) for magnetic fields up to 100 T. We point out that ultrahigh magnetic fields on the order of hundreds of teslas can be achieved at a number of pulsed magnetic field facilities [58–60].

The spin-up and spin-down states are shown as solid and dashed lines, respectively. (We use "spin-up" and "spin-down" for the hole states to denote the J_z component, not the true spin S_z.) Note that while there is a break in the energy axis, the energy scales are the same before and after the break. The conduction states are pure spin-up and spin-down states with $J_z = \pm\frac{1}{2}$. At high fields, we notice a bowing in the conduction band energy levels due to the $\mathbf{A}^2$ terms in the Landau Hamiltonian in Eq. (A4). There are two predominantly heavy-hole and two predominantly light-hole states. Because of coupling between states in the 6×6 valence band effective mass Hamiltonian, the hole states are mixed. For the lowest-lying heavy and light holes the states are better than 99.0% pure, while the excited hole states can exhibit much greater mixing.

At low magnetic fields, the magnetic-field-induced energy level splitting is proportional to the magnetic field (parallel to z) and can be described by effective magnetic g factors. By definition, the effective g factor is given by

$$g = \frac{E_\uparrow(B) - E_\downarrow(B)}{2\,|J_z|\,\mu_B B}, \tag{2}$$

where $E_\uparrow(B) - E_\downarrow(B)$ is the energy level splitting between spin-up and spin-down states, $|J_z|$ is the absolute value of the z component of the spin, B is the external magnetic field, and $\mu_B = 5.789 \times 10^{-5}$ eV/T is the Bohr magneton. In Fig. 7(a) the effective g factors are 2.0 for the conduction band states and 0.845 for both the heavy- and light-hole states. The heavy-hole

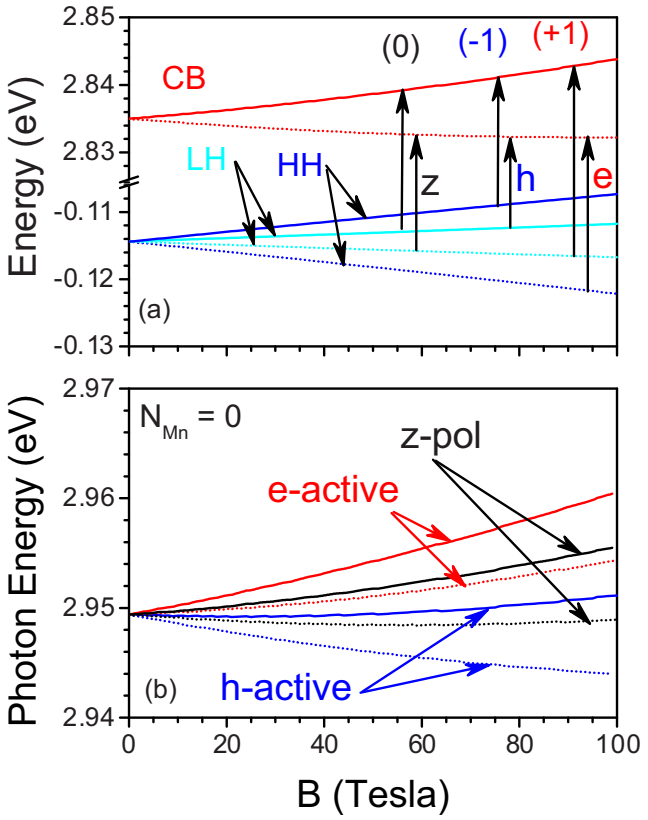

FIG. 7. Energy levels (a) and transition energies (b) as functions of an applied magnetic field B for the lowest-lying conduction electron (CB) and valence heavy-hole (HH) and light-hole (LH) states in an undoped 100 Å diameter ($R = 50$ Å) CdS-ZnS spherical core-shell quantum dot with a 50 Å diameter ($R_c = 25$ Å) CdS core. In (a) the spin-up and spin-down states are solid and dotted lines, respectively. Dipole-allowed transitions for circularly polarized e-active (σ_+), circularly polarized h-active (σ_-), and z-linear polarized light are indicated by vertical arrows labeled e, h, and z, respectively. The numbers in parentheses are the angular momentum changes between initial and final states. In (b) transition energies for transitions to the first spin-up conduction state are solid lines while transitions to the first spin-down conduction state are dotted lines.

splitting is three times greater than the light-hole splitting since $|J_z| = \frac{3}{2}$ for heavy holes and $|J_z| = \frac{1}{2}$ for light holes.

In our study of optical properties, we considered positive helicity e-active (σ_+) and negative helicity h-active (σ_-) circularly polarized light incident on the core-shell nanoparticle parallel to z, i.e., the direction of the applied magnetic field. The dipole-allowed e-active and h-active transitions are indicated by vertical arrows in Fig. 7(a). The numbers in parentheses above these arrows are the angular momentum changes between the initial hole state and final electron state. For example, there is an h-active (σ_-) transition between the heavy-hole spin-up $J_z = \frac{3}{2}$ state and the electron spin-up $J_z = \frac{1}{2}$ state with a resulting momentum change of $\Delta J_z = -1$. Likewise, there is an e-active (σ_+) transition between the light-hole spin-down $J_z = -\frac{1}{2}$ state and the electron spin-up $J_z = \frac{1}{2}$ state with $\Delta J_z = +1$.

We have also considered linear polarization with the electric field polarization vector in the xy plane (denoted x polarization) and parallel to magnetic field (denoted z polarization). In the case of z polarization, the direction of propagation is perpendicular to the magnetic field and the angular momenta for the initial and final states satisfy $\Delta J_z = 0$. In this case, only transitions between light holes and electrons with the same spin are dipole allowed. In the case of linear polarization in the xy plane, the angular momentum selection rule is $\Delta J_z = \pm 1$.

The dipole-allowed transition energies for e-active, h-active, and z-polarized absorption are shown in Fig. 7(b). The line styles are determined by the final state. Transition energies for transitions to the spin-up conduction state are solid lines while transition energies for transitions to the spin-down conduction state are shown as dotted lines. In the case of linear polarization in the xy plane, the transition energies are the union of the dipole-allowed transition energies for both e- and h-active polarization ($\Delta J_z = \pm 1$) giving rise to four dipole-allowed transitions.

For low magnetic fields, the transition energy, $E_T(B)$, as a function of the applied magnetic field, B, can be estimated from the transition energy in the absence of a magnetic field, E_0, and the g factors and spin quantum numbers, J_z, of the dipole-allowed initial and final states. The transition energies at low fields are given by

$$E_T(B) = E_0 + \left(J_z^c g_c - J_z^v g_h\right)\mu_B B, \tag{3}$$

where J_z^c and J_z^v are the angular momenta for the conduction and valence band levels, g_c and g_h are the corresponding electron and hole effective g factors, and μ_B is the Bohr magneton.

The absorption spectrum as a function of photon energy and polarization was obtained from Fermi's golden rule with the delta function in Eq. (A36) replaced by a Lorentzian with a full width at half maximum (FWHM) of 2 meV. Contour plots of absorption spectra for undoped 100 Å diameter ($R = 50$ Å) CdS-ZnS spherical core-shell quantum dots with a 50 Å diameter ($R_c = 25$ Å) CdS cores are shown in Fig. 8 for magnetic fields up to 100 T.

In Fig. 8(a) the light is assumed to be h-active circularly polarized. We observe two strong dipole-allowed transitions labeled C1-V2 and C2-V1. In this notation, C1 and C2 are the first two conduction states with spin-down and spin-up, respectively. The first four valence states (V1–V4) are, respectively, heavy-hole spin-up (V1), light-hole spin-up (V2), light-hole spin-down (V3), and heavy-hole spin-down (V4). The stronger of the two transitions, C2-V1, is a heavy-hole transition while the weaker transition, C1-V2, is a light-hole transition. The transition energy shift for the heavy-hole C2-V1 transition as a function of magnetic field is less than the corresponding transition energy shift for the C1-V2 transition. The reason for this is seen in the fan diagram in Fig. 7(a). The initial and final states in the C2-V1 heavy-hole transition are spin-up states and hence initial and final states are both shifted to higher energies by the magnetic field. These two energy levels in the fan diagram are nearly parallel leading to a lower transition energy shift in spite of the fact that the heavy-hole levels themselves are shifted more.

In Fig. 8(b) the light is assumed to be e-active circularly polarized and here we also observe two strong dipole-allowed transitions labeled C1-V4 and C2-V3. Again, the stronger

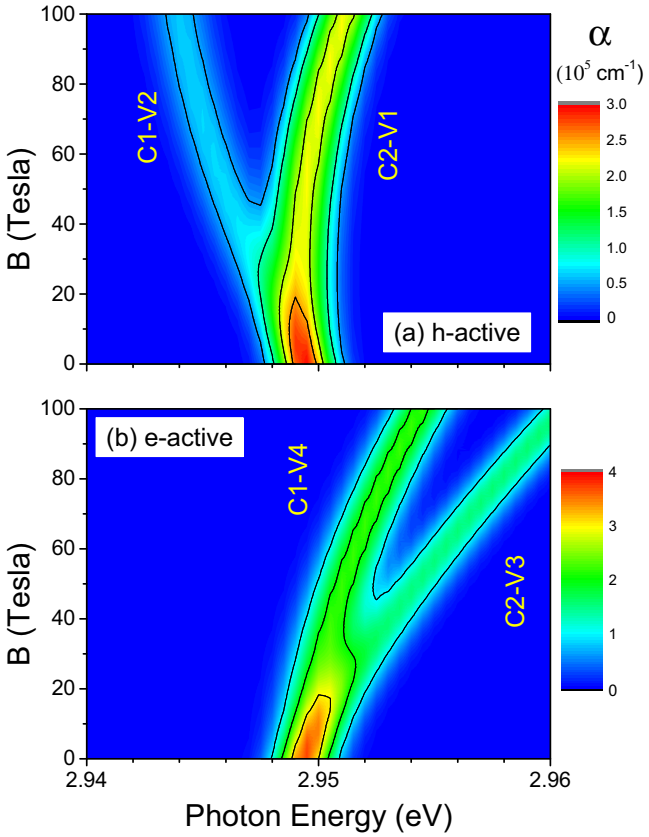

FIG. 8. Contour plot of absorption spectra for an undoped 100 Å diameter ($R = 50$ Å) CdS-ZnS spherical core-shell quantum dot with a 50 Å diameter ($R_c = 25$ Å) CdS core in applied magnetic fields up to 100 T. The photon polarizations are (a) h active (σ_-) and (b) e active (σ_+), and the FWHM linewidths are all assumed to be 2 meV. Transitions are labeled by conduction and valence state indices relative to the band edge as described in the text.

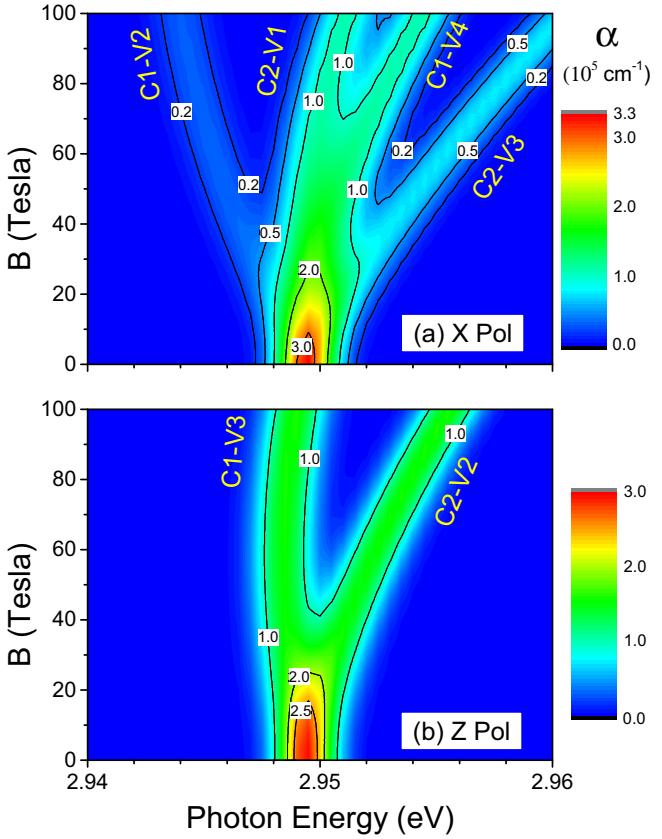

FIG. 9. Contour plot of absorption spectra for an undoped 100 Å diameter ($R = 50$ Å) CdS-ZnS spherical core-shell quantum dot with a 50 Å diameter ($R_c = 25$ Å) CdS core in applied magnetic fields up to 100 T. The photon polarizations are (a) X-linear polarized and (b) Z polarized and the FWHM linewidths are all assumed to be 2 meV. Transitions are labeled by conduction and valence state indices relative to the band edge as described in the text.

transition is a heavy-hole transition while the weaker one is a light-hole transition. Likewise, the heavy-hole transition energy shift is less than the light-hole transition energy shift.

We have also calculated absorption spectra for linearly polarized light as a function of applied magnetic field. We considered linearly polarized light propagating in the direction of the applied magnetic field, B, with the electric field polarization vector perpendicular to B in the xy plane referred to as X polarization. Additionally we also considered linearly polarized light propagating perpendicular to the applied magnetic field B with the electric field polarization vector parallel to B in the z direction referred to as Z polarization.

Contour plots of absorption spectra for undoped 100 Å diameter CdS-ZnS spherical core-shell quantum dots with 50 Å diameter CdS cores are shown in Fig. 9 for magnetic fields up to 100 T and linearly polarized light. Results for X-polarized light are shown in Fig. 9(a). There are four dipole-allowed transitions C1-V2, C2-V1, C1-V4, and C2-V3 in order of increasing energy which satisfy the selection rule $\Delta J_z = \pm 1$. These transitions are, in order of increasing energy, light-hole spin-up, heavy-hole spin-up, heavy-hole spin-down, and light-hole spin-down. Results for Z-polarized light are shown in Fig. 9(b). Here there are only two dipole-allowed transitions C1-V3 and C2-V2 in order of increasing energy which satisfy the selection rule $\Delta J_z = 0$. These transitions are, respectively, light-hole spin-down and light-hole spin-up.

B. Mn-doped CdS-ZnS nanoparticles

To illustrate the effect of localized Mn doping on the energy levels and transition energies shown in Fig. 7, we performed a similar calculation but with two Mn impurities at the center of the CdS core. The results are shown in Fig. 10. To facilitate comparison, we plotted everything on the same scales in both figures. Comparing Fig. 7(a) and Fig. 10(a), we notice that the spin splitting for the conduction levels is *suppressed* while the spin splitting for the heavy-hole and light-hole levels has been *enhanced*. At low magnetic fields, the effective g factor for the electrons decreases from $g = 2.0$ to $g = 1.82$ while the g factors for heavy and light holes both increase from $g = 0.845$ to $g = 1.78$. This behavior can be traced to the fact that the Mn s-d exchange integral ($N_0\,\alpha > 0$) and the p-d exchange integral ($N_0\,\beta < 0$) used in our model have different signs. Due to the antiparallel orientation of B and the average spin $\langle S_z \rangle$ in Mn, an exchange integral with a positive sign results in g-factor reduction while an exchange

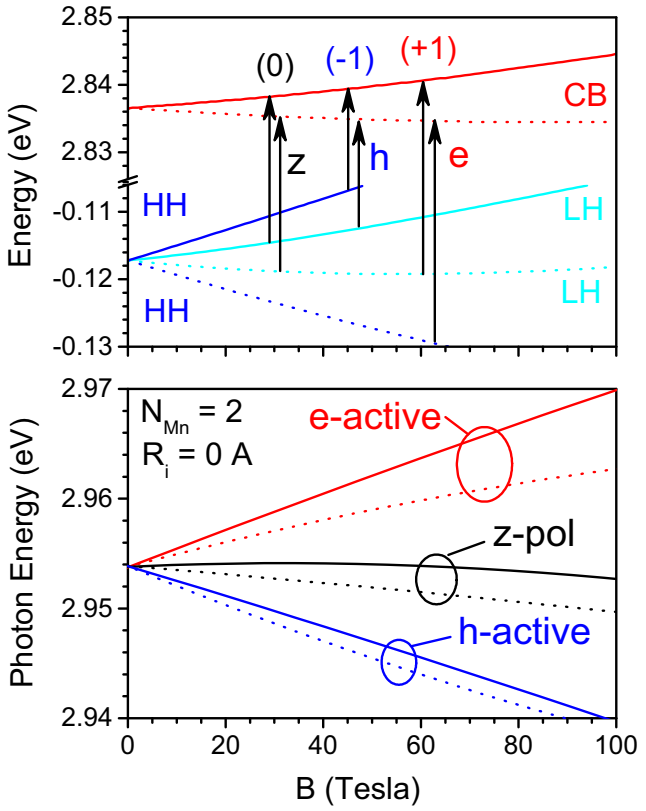

FIG. 10. Energy levels (a) and transition energies (b) as functions of an applied magnetic field B for the lowest-lying conduction and valence bands in a 100 Å diameter ($R = 50$ Å) CdS-ZnS spherical core-shell quantum dot with a 50 Å diameter ($R_c = 25$ Å) CdS core and two Mn impurities at the center of the core. In (a) the spin-up and spin-down states are solid and dotted lines, respectively. Dipole-allowed transitions for e-active (σ_+) and h-active (σ_-) circularly polarized light and z-linear polarized light are indicated by vertical arrows. The numbers in parentheses are the angular momentum changes between initial and final states. In (b) transition energies for transitions to the first spin-up conduction state are solid lines while transitions to the first spin-down conduction state are dotted lines.

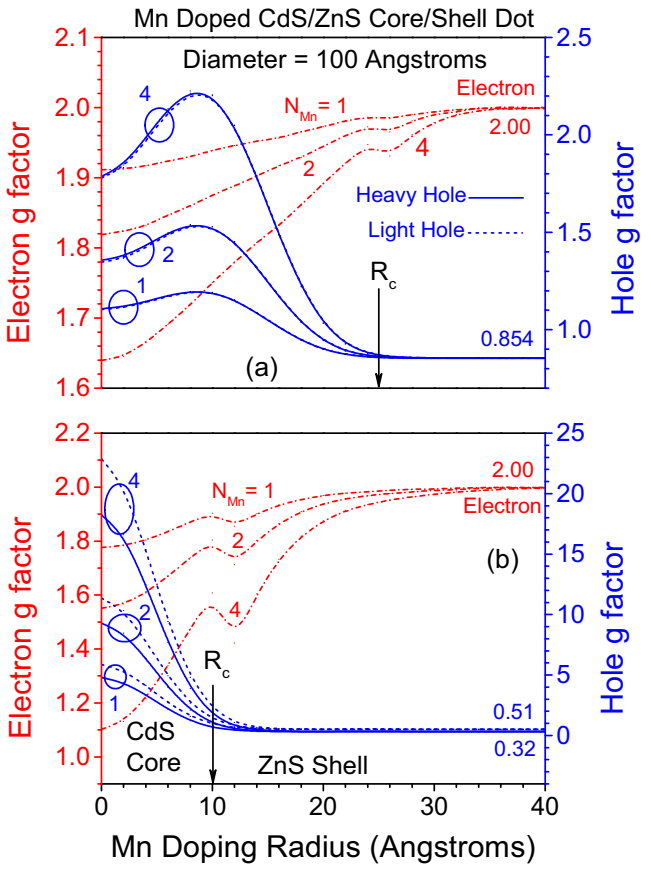

FIG. 11. Magnetic g factors at $T = 300$ K for the lowest-lying electron (red dot dashed), heavy-hole (solid blue), and light-hole (dashed blue) levels in Mn radial position doped 100 Å diameter ($R = 50$ Å) CdS-ZnS spherical core-shell quantum dots as a function of Mn doping radius for 1, 2, and 4 Mn dopants per dot. In (a) the CdS core radius $R_c = 25$ Å while in (b) $R_c = 10$ Å.

integral with a negative sign increases the g factor. If we compare the transition energies in Fig. 7(b) and Fig. 10(b), we find that the splitting between e-active and h-active transition energies is enhanced while the splitting between transitions to the lowest spin-up and spin-down electron levels is suppressed. In addition the curvature of the transition energies with magnetic field bends downward when Mn impurities are added.

We calculated magnetic g factors at room temperature for the lowest-lying electron, heavy-hole, and light-hole levels as a function of doping radius in ensembles of Mn radial position doped 100 Å diameter ($R = 50$ Å) CdS-ZnS core-shell nanoparticles with either 50 Å or 20 Å diameter CdS cores. The Mn dopants in the ensemble are treated in the virtual crystal approximation where the Mn impurity Hamiltonian is treated as if all the dopants were smeared out uniformly over an infinitely thin doping shell or radius R_i. We find that Mn doping enhances the heavy-hole and light-hole g factors while suppressing the electron g factors. In fact, with high enough Mn doping, one can change the sign of the electron g factor as seen in InMnAs for high Mn doping [61]. In general, the Mn impurity interaction with a quantum dot state is large when there is a large overlap between its effective mass envelope function and the Mn impurities.

Our results are shown in Fig. 11. Three sets of curves are shown corresponding to 1, 2, and 4 Mn dopants per nanoparticle. The Mn doping can dramatically alter the magnetic g factors which are found to be sensitive to the core radius and the Mn doping radius. In Fig. 11(a), the core radius $R_c = 25$ Å. For the lowest-lying electron levels, the largest change in the g factors is obtained by doping in the core center. The g factors for the lowest-lying heavy-hole and light-hole levels are nearly degenerate and the largest enhancement in the g factors is obtained for a Mn doping radius of approximately 10 Å. For a given number of Mn impurities, the g factor changes are strongest within the CdS core and decrease sharply at the core-shell boundary, R_c. At the surface of the quantum dot the Mn impurity Hamiltonian vanishes and the g factors return to their undoped values. The reason for this is that the effective mass envelope functions vanish at the quantum dot

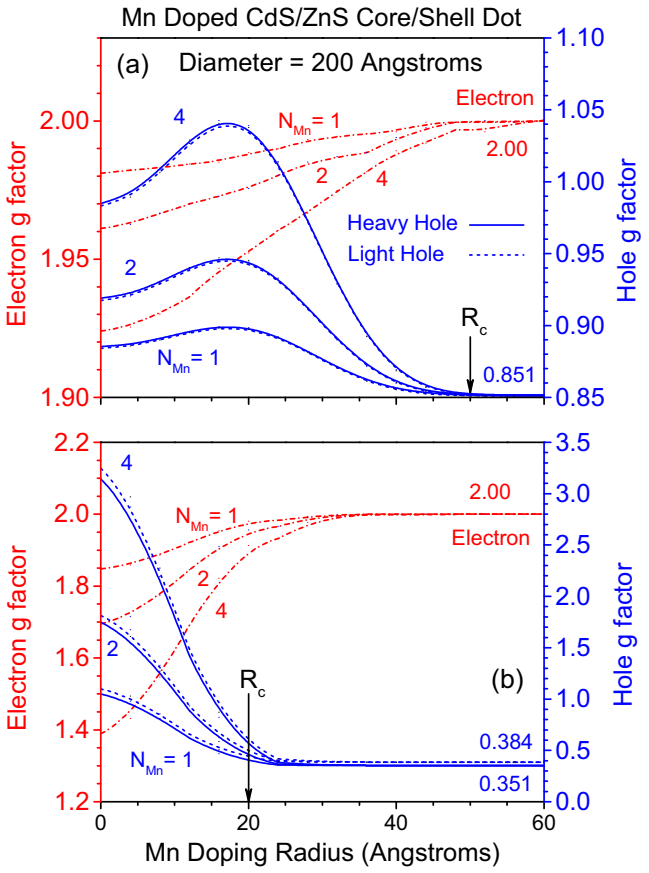

FIG. 12. Magnetic g factors at $T = 300$ K for the lowest-lying electron (red dot dashed), heavy-hole (solid blue), and light-hole (dashed blue) levels in Mn radial position doped 200 Å diameter ($R = 100$ Å) CdS-ZnS core-shell quantum dots as a function of Mn doping radius for 1, 2, and 4 Mn dopants per dot. In (a) the CdS core radius $R_c = 50$ Å while in (b) $R_c = 20$ Å.

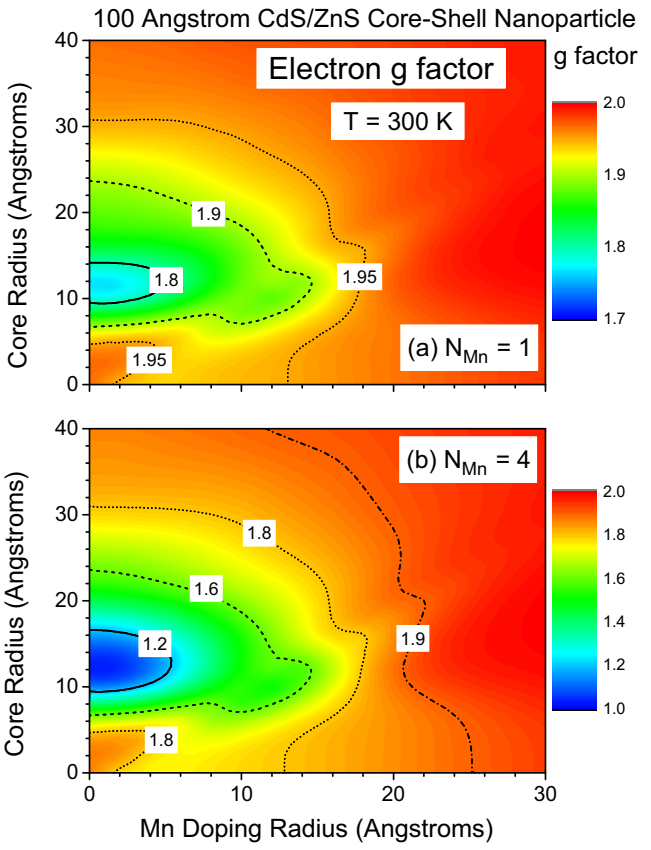

FIG. 13. Electron magnetic g factor in Mn radial position doped 100 Å diameter ($R = 50$ Å) CdS-ZnS spherical core-shell quantum dots as a function of CdS core radius and Mn doping radius for (a) one Mn dopant and (b) four Mn dopants per quantum dot. Note different color scales.

surface and hence cannot overlap with an infinitely thin Mn doping shell at the surface.

The effect of decreasing the core radius from $R_c = 25$ Å to $R_c = 10$ Å is shown in Fig. 11(b). For the undoped nanoparticle, the g factors are 2.0 for electrons and the heavy-hole and light-hole g factors are split with 0.32 and 0.51 for heavy holes and light holes respectively. The changes in the g factors are greatest for Mn doping within the core and more pronounced. In particular, the hole g factors are greatest for Mn doping at the center of the core and are much larger. From Fig. 11 we see that with 4 Mn impurities per nanoparticle, the heavy-hole g factor goes from a maximum of 2.2 for $R_c = 25$ Å to 18.0 for $R_c = 10$ Å.

We also calculated room temperature magnetic g factors for the lowest-lying electron, heavy-hole, and light-hole levels as a function of Mn doping radius in 200 Å diameter ($R = 100$ Å) CdS-ZnS spherical core-shell nanoparticles with either 100 Å or 40 Å diameter CdS cores. The results are shown in Fig. 12 and are qualitatively similar to the results in Fig. 11 discussed earlier.

C. Structure-property relationships

To extend these ideas and increase their utility, we developed structure-property relations for electron and heavy-hole g factors in 100 Å and 200 Å diameter CdS-ZnS spherical core-shell quantum dots with either one or four Mn impurities per nanoparticle. These scenarios are summarized in the contour plots of Figs. 13–20. While details of our model can still be improved upon, we expect these trends to be obeyed.

We begin by discussing electron g factors. Figure 13 displays electron g factor as a function of Mn doping radius and CdS core radius with temperature fixed at $T = 300$ K in a 100 Å diameter ($R = 50$ Å) CdS-ZnS core-shell nanoparticle for two different Mn impurity numbers. For a given number of Mn impurities, the room temperature electron g factor varies from a maximum of $g = 2$ for large Mn doping radii to a minimum value near the center of the CdS core. The largest reduction in the electron g factor is achieved with a CdS core radius of approximately $R_c = 12$ Å. With the optimal CdS core radius and four Mn impurities per nanoparticle, we see that the electron g factor can be cut nearly in half.

Figure 14 displays room temperature electron g factors in a 200 Å diameter ($R = 100$ Å) CdS-ZnS core-shell nanoparticle as a function of Mn doping radius and CdS core radius for two different Mn impurity numbers. The structure-property

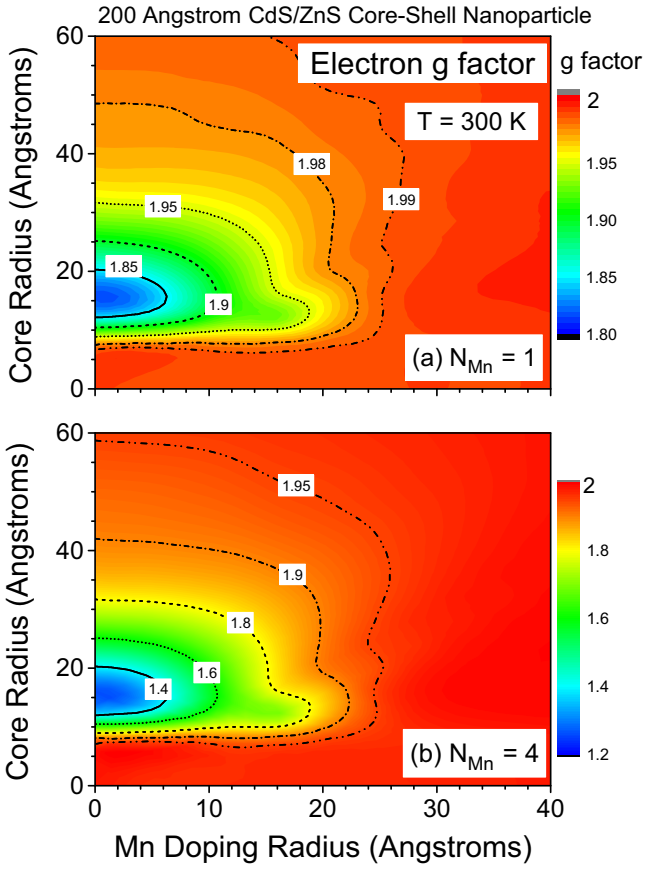

FIG. 14. Electron magnetic g factor in Mn radial position doped 200 Å diameter CdS-ZnS spherical core-shell quantum dots as a function of CdS core radius and Mn doping radius for (a) one Mn dopant and (b) four Mn dopants per quantum dot. Note different color scales.

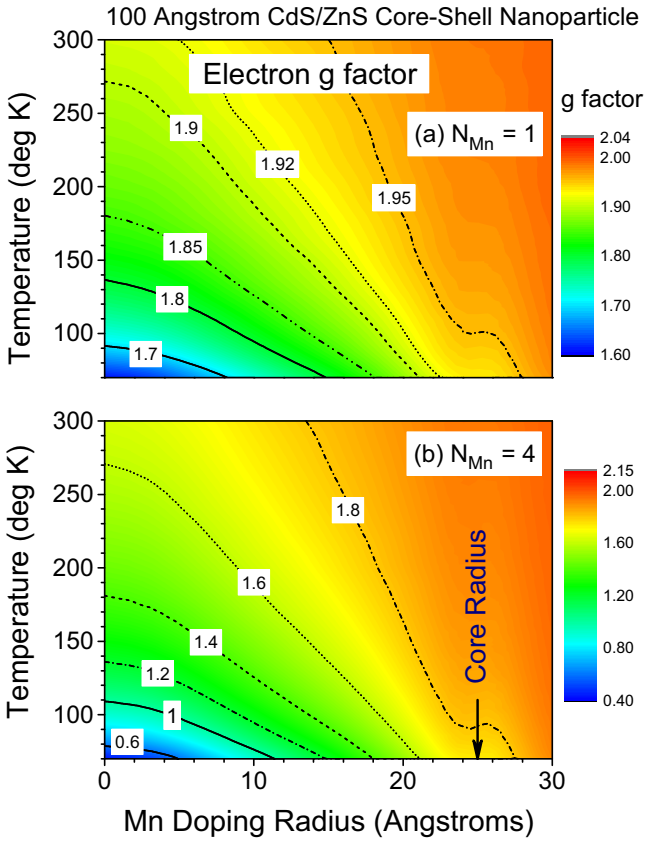

FIG. 15. Magnetic g factors for the lowest-lying electron levels in 100 Å CdS-ZnS diameter ($R = 50$ Å) spherical core-shell quantum dots with a 50 Å diameter ($R_c = 25$ Å) CdS core as a function of Mn doping radius and temperature for (a) one Mn dopant and (b) four Mn dopants per nanoparticle.

relations for the 100 Å and 200 Å diameter nanoparticle are qualitatively similar. The room temperature electron g factor varies from a maximum of $g = 2$ at large Mn doping radii to a minimum near the center of the CdS core. However, the reduction of the electron g factor in the 200 Å diameter nanoparticle is not as great. The largest reduction in the electron g factor is achieved in a 200 Å diameter ($R = 100$ Å) CdS-ZnS nanoparticle with a CdS core radius of approximately $R_c = 15$ Å.

Figures 15 and 16 display contour plots of the electron g factor as a function of Mn doping radius and temperature in 100 Å ($R = 50$ Å) and 200 Å diameter ($R = 100$ Å) CdS-ZnS core-shell nanoparticles. In both cases, the CdS core radius is $R_c = R/2$. In general, lowering the temperature reduces the electron g factor with the greatest reduction occurring for Mn doping at the center of the CdS core.

The trends in Figs. 13–16 can be qualitatively understood by means of a simple analytical calculation. We estimate the effective electron g factor by assuming that (1) the Mn impurities are uniformly distributed in the CdS core, (2) the electrons are completely confined in the core with no tunneling into the shell, and (3) changes in the effective g factor from the bulk value of 2 are entirely determined by the s-d exchange interaction between the itinerant electrons and the Mn d electrons. As shown in the Appendix, the effective electron g factor is approximately

$$g \approx 2 - \frac{35\,N_i}{32\,\pi}\,\frac{N_0\alpha}{k_B T}\left(\frac{a}{R_c}\right)^3, \tag{4}$$

where $a = 5.81$ Å is the core lattice constant, R_c is the core radius, $N_0\alpha = 0.22$ eV is the s-d exchange interaction, $k_B T$ is the thermal energy, and N_i is the number of Mn impurities in the core. This simple model can be compared with the more elaborate calculation in the case where the Mn doping radius $R_i \approx 0$. Our approximate electron g-factor formula illustrates several qualitative results. First, the introduction of Mn impurities in the core acts to *reduce* the electron magnetic g factor from its bulk value of $g = 2$. Second, the reduction in the electron g factor is directly proportional to the number of Mn impurities and inversely proportional to the lattice temperature and the cube of the core radius. If we assume a nanoparticle with a 50 Å diameter CdS core and four Mn impurities *uniformly distributed* throughout the core at a temperature of $T = 300$ K, we obtain $g = 1.87$ for the electron magnetic g factor. This crude result is similar to the $g = 1.64$ obtained in the more elaborate calculation assuming four Mn impurities *at the center* of the CdS core ($R_i = 0$) as can be read off in Fig. 11(a).

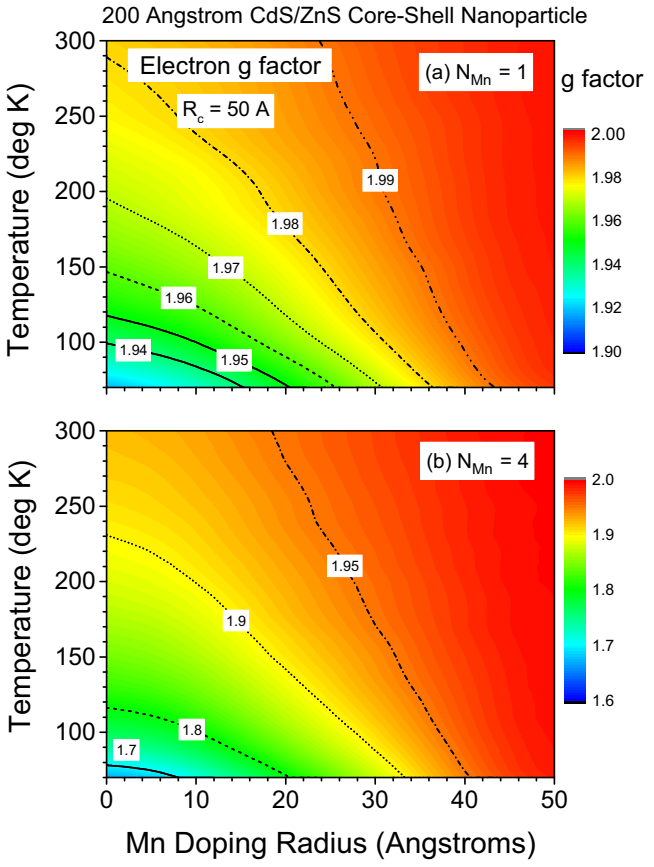

FIG. 16. Magnetic g factors for the lowest-lying electron levels in 200 Å CdS-ZnS diameter ($R = 100$ Å) spherical core-shell quantum dots with a 100 Å diameter ($R_c = 50$ Å) CdS core as a function of Mn doping radius and temperature for (a) one Mn dopant and (b) four Mn dopants per nanoparticle.

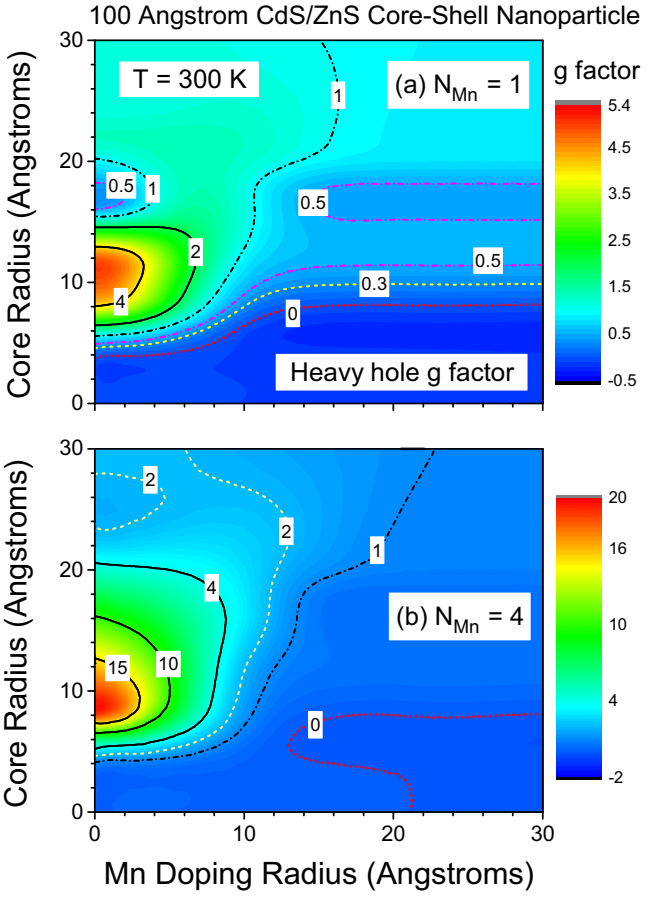

FIG. 17. Heavy-hole magnetic g factor in Mn radial position doped 100 Å diameter ($R = 50$ Å) CdS-ZnS spherical core-shell quantum dots as a function of CdS core radius and Mn doping radius for (a) one Mn dopant and (b) four Mn dopants per quantum dot.

The heavy-hole g factors are more complicated due the sixfold valence band degeneracy and strong interactions between heavy, light, and split-off holes. In Figs. 17 and 18 the heavy-hole g factor at room temperature is shown as a function of the Mn doping radius and the CdS core radius. The resulting structure-property diagrams for heavy-hole g factors are richer and more complex. For instance, there are places in the (R_i, R_c) plane where the heavy-hole g factor can be zero or even negative. In general, negative heavy-hole g factors can only occur in core-shell nanoparticles with very small CdS cores. Depending on the number of Mn impurities in the nanoparticle, the heavy-hole g factor can become rather large. With four Mn impurities per nanoparticle, the heavy-hole g factor in a 100 Å diameter quantum dot can approach 20 if the CdS core radius $R_c \approx 10$ Å. In a 200 Å diameter ($R = 100$ Å) nanoparticle with four Mn impurities, the heavy-hole g factor is around 3 if the CdS core radius $R_c \approx 20$ Å.

In Figs. 19 and 20 we plot structure-property diagrams of the heavy-hole g factors in 100 Å ($R = 50$ Å) and 200 Å diameter ($R = 100$ Å) core-shell quantum dots as functions of Mn doping radius and temperature for two different Mn impurity numbers. In Fig. 19 the particle radius is $R = 100$ Å, the CdS core radius is $R_c = 25$ Å, and the heavy-hole g factor is plotted as a function of Mn doping radius and temperature. We find that lowering the temperature increases the heavy-hole g factor. In addition, we see that the greatest g-factor enhancement occurs when the Mn doping radius is around 10 Å. Surprisingly, reducing the temperature does not always increase the g factor. In Fig. 19(b), we see that with four Mn impurities per nanoparticle positioned at the center of the CdS core, the heavy-hole g factor initially *increases* to $g = 2$ as the temperature is lowered from room temperature to $T \approx 195$ K and thereafter decreases and finally becomes negative as the temperature is lowered to liquid nitrogen temperatures ($T = 77$ K).

We can attempt a qualitative analysis of the heavy-hole g factor in a 100 Å diameter ($R = 50$ Å) CdS-ZnS core-shell nanoparticle with a 50 Å diameter ($R_c = 25$ Å) core along the same lines as we did for the electron g factors. Details are provided in the Appendix. Keeping in mind that $J_z = \frac{3}{2}$ for heavy holes as opposed to $J_z = \frac{1}{2}$ for electrons, we obtain the approximate expression

$$g \approx g_h - \frac{35}{96}\frac{N_i}{\pi}\frac{N_0\beta}{k_B T}\left(\frac{a}{R_c}\right)^3, \tag{5}$$

where g_h is the hole g factor for $N_i = 0$ and $N_0\beta = -1.8$ eV is the p-d exchange interaction. Since the p-d exchange interaction is negative, the introduction of Mn impurities

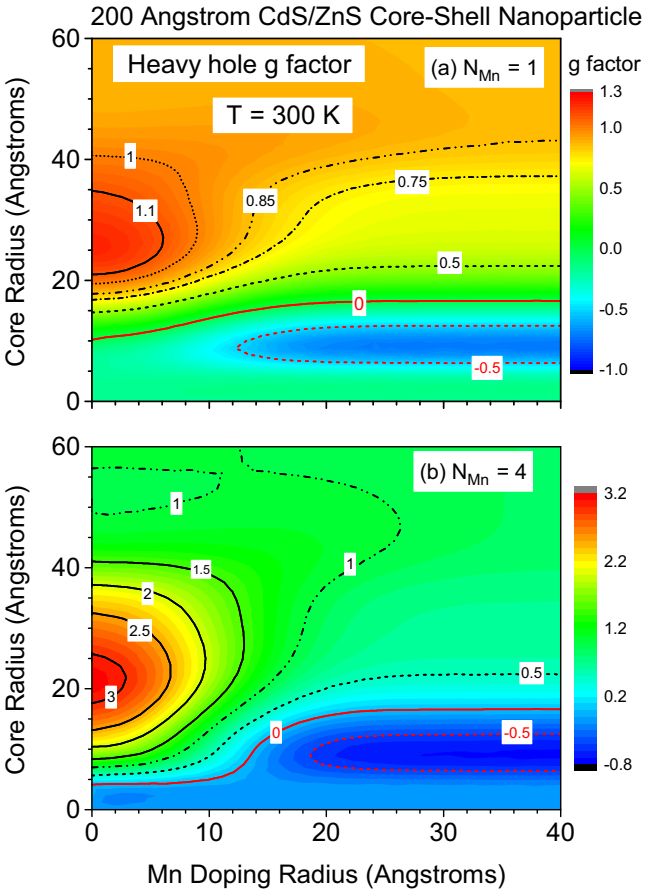

FIG. 18. Heavy-hole magnetic g factor in Mn radial position doped 200 Å diameter ($R = 100$ Å) CdS-ZnS spherical core-shell quantum dots as a function of CdS core radius and Mn doping radius for (a) one Mn dopant and (b) four Mn dopants per quantum dot.

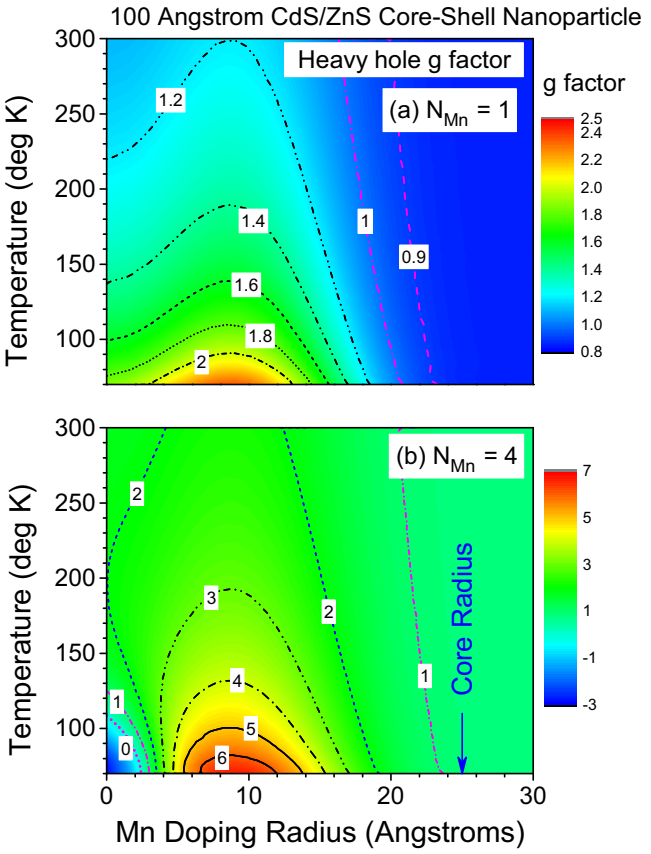

FIG. 19. Magnetic g factors for the lowest-lying heavy-hole levels in 100 Å diameter ($R = 50$ Å) CdS-ZnS spherical core-shell quantum dots with 50 Å diameter ($R_c = 25$ Å) CdS core as a function of Mn doping radius and temperature for (a) one Mn dopant and (b) four Mn dopants per nanoparticle.

tends to increase the heavy-hole g factor. Taking $g_h \approx 0.854$ from the more elaborate calculation, we obtain a heavy-hole magnetic g factor of $g = 1.22$ for a nanoparticle with a 50 Å diameter ($R_c = 25$ Å) CdS core and four Mn impurities uniformly distributed in the core at room temperature. This compares with $g = 2.2$ obtained for Mn impurities concentrated at the center of the CdS core as seen in Fig. 11(a) which is more of a discrepancy in comparison with electron case.

It would be nice to compare these structure-property relations with experiment to validate our model. In Ref. [62] similar trends can be seen in core-shell ZnSe-CdSe nanoparticles with ZnSe cores uniformly doped with magnetic Cu^{2+} impurities [62]. Magnetic circular dichroism (MCD) studies on these nanoparticles have been carried out in magnetic fields up to 4 T for temperatures ranging from 1.7 K to 40 K. The MCD data on these nanoparticles indicates that the Cu^{2+} impurities do in fact behave as paramagnetic *sp-d* active dopants.

IV. SUMMARY AND OUTLOOK

Controlled magnetic impurity doping in dilute magnetic semiconductor core-shell nanoparticles provides great opportunities for engineering magnetic g factors and magneto-optical properties in crystals that can prove useful in potential spintronic applications. To date however, no theory of electronic states, g factors, and magneto-optical properties in core-shell nanoparticles with position-controlled magnetic impurity doping has been presented. To remedy this situation, we developed an effective mass theory for electronic and magneto-optical properties of spherical core-shell nanoparticles and tested our predictions on the Mn-doped CdS-ZnS system—a system that has been fabricated experimentally.

We calculated magnetic g factors for the lowest-lying electron levels and the lowest-lying heavy- and light-hole levels as a function of the number of Mn dopants per nanoparticle, the Mn doping radius, and the temperature, and have identified a number of qualitative trends. We find that Mn doping increases the heavy- and light-hole g factors while reducing g factors for electrons. The Mn impurity interaction with a nanoparticle state is large when there is a significant overlap between its effective mass envelope function and the Mn impurity doping shell. For the lowest-lying electron and hole levels, the largest change in the g factors is obtained by doping in the center of the optically active CdS core. The overlap between the envelope function and the Mn impurities can be tuning by varying the radius of the CdS core. As a general rule, lowering the temperature tends to lower the electron g factor and increase the hole g factor. Strain due

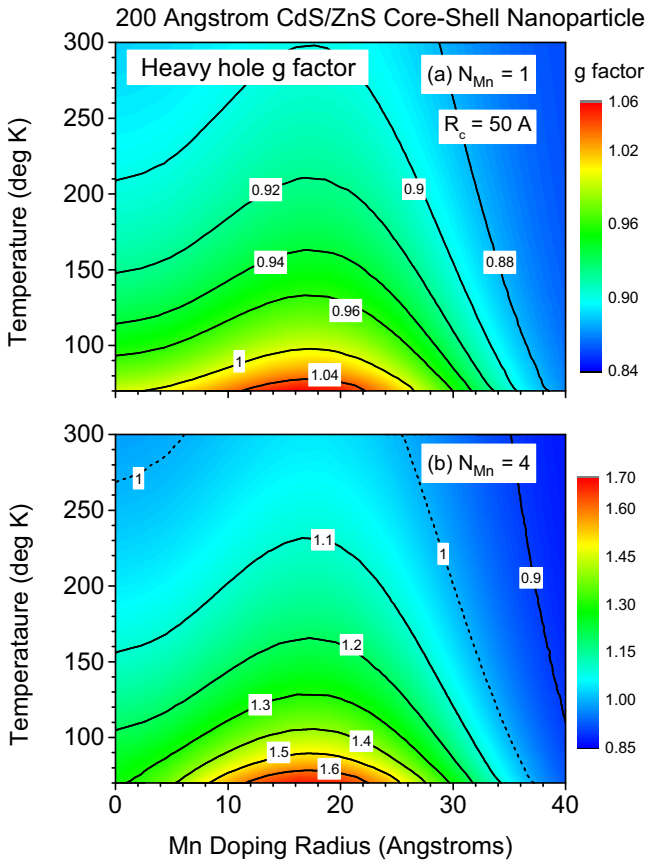

FIG. 20. Magnetic g factors for the lowest-lying heavy-hole levels in 200 Å diameter ($R = 100$ Å) CdS-ZnS spherical core-shell quantum dots with a 100 Å diameter ($R_c = 50$ Å) CdS core as a function of Mn doping radius and temperature for (a) one Mn dopant and (b) four Mn dopants per nanoparticle.

to lattice mismatch at the core-shell interface also effects the magneto-optical properties of core-shell nanoparticles. We find that the major effect of pseudomorphic strain is to rigidly shift the lowest-lying transitions to higher photon energies.

Our calculations demonstrate the potential of magnetically doped core-shell nanoparticles in future spintronic device applications such as q-bits and transfer torque devices. Moreover, the platform that we have developed can be used a tool for designing g-factor-engineered nanostructures. Looking forward, our methodology can be extended to more complex structures with arbitrary multiple semiconductor onion shells and arbitrary magnetic impurity doping profiles with various magnetic impurities. In addition, engineering magnetic g factors and magneto-optical properties in quantum well and quantum wire geometries can also be explored.

ACKNOWLEDGMENTS

We thank Professor Y. Charles Cao of the University of Florida Chemistry Department for suggesting we extend our earlier work on magnetically doped semiconductor quantum well structures to the problem of core-shell quantum dots. Work at the University Florida was partially supported by the Office of Research at the University of Florida and by the the National Science Foundation through Grant No. DMR 1311849 and partially by the AFOSR through Grant No. FA9550-14-1-0376. Research at Tennessee was supported by the Materials Science Division, Basic Energy Sciences, US Department of Energy, under Award No. DE-FG02-01ER45885.

APPENDIX A: COMPUTATIONAL DETAILS

1. Effective mass formalism

The effective mass Hamiltonian for the Mn-doped core-shell nanoparticle in a magnetic field directed along the z axis is just the sum of the Landau, Zeeman, strain, and sp-d exchange contributions, i.e.,

$$H = H_L + H_Z + H_S + H_{\mathrm{Mn}}. \tag{A1}$$

We assume the core and shell are wide-gap zinc-blende semiconductors and we ignore the coupling between conduction and valence bands in the effective mass Hamiltonian. This is valid for wide-gap materials, but can be extended to narrow-gap semiconductors. The material parameters used in this work are shown in Table I. In our core-shell quantum dot model, all the effective mass parameters listed in Table I are piecewise constant r-dependent functions. For example, the position-dependent band gap $E_g(r)$ is 2.5 eV in the CdS core ($0 < r < R_c$) and 3.54 eV in the ZnS shell ($R_c < r < R$).

Following the convention of Pidgeon and Brown [63], the eight Bloch basis states for conduction and valence electrons can be separated into an upper and lower set which decouple at the zone center, i.e., $k_z = 0$. The Bloch basis states for the upper set are

$$|1\rangle = \left|\tfrac{1}{2}, +\tfrac{1}{2}\right\rangle = |S\uparrow\rangle, \tag{A2a}$$

$$|2\rangle = \left|\frac{3}{2}, +\frac{3}{2}\right\rangle = \frac{1}{\sqrt{2}}|(X+iY)\uparrow\rangle, \tag{A2b}$$

$$|3\rangle = \left|\frac{3}{2}, -\frac{1}{2}\right\rangle = \frac{1}{\sqrt{6}}|(X-iY)\uparrow +2Z\downarrow\rangle, \tag{A2c}$$

$$|4\rangle = \left|\frac{1}{2}, -\frac{1}{2}\right\rangle = \frac{i}{\sqrt{3}}|-(X-iY)\uparrow +Z\downarrow\rangle, \tag{A2d}$$

which correspond to electron spin-up, heavy-hole spin-up, light-hole spin-down, and split-off hole spin-down. Likewise, the Bloch basis states for the lower set are

$$|5\rangle = \left|\tfrac{1}{2}, -\tfrac{1}{2}\right\rangle = |S\downarrow\rangle, \tag{A3a}$$

$$|6\rangle = \left|\frac{3}{2}, -\frac{3}{2}\right\rangle = \frac{i}{\sqrt{2}}|(X-iY)\downarrow\rangle, \tag{A3b}$$

$$|7\rangle = \left|\frac{3}{2}, +\frac{1}{2}\right\rangle = \frac{i}{\sqrt{6}}|(X+iY)\downarrow -2Z\uparrow\rangle, \tag{A3c}$$

$$|8\rangle = \left|\frac{1}{2}, +\frac{1}{2}\right\rangle = \frac{1}{\sqrt{3}}|(X+iY)\downarrow +Z\uparrow\rangle, \tag{A3d}$$

corresponding to electron spin-down, heavy-hole spin-down, light-hole spin-up, and split-off hole spin-up.

The total effective mass Hamiltonian for conduction and valence electrons is the sum of four Hamiltonians. These are

TABLE I. Parameters for $Cd_{1-x}Mn_xS$ and $Zn_{1-x}Mn_xS$.

Parameter	$Cd_{1-x}Mn_xS$	$Zn_{1-x}Mn_xS$
Direct band gap (eV)		
E_g	2.5[a]	3.54[b]
Spin orbit splitting (eV)		
Δ	0.08[a]	0.07[c]
Electron effective mass		
m_e^* (m_0)	0.15[a]	0.28[c]
Luttinger parameters		
γ_1	0.814[a]	2.54[c]
γ_2	0.307[a]	0.75[c]
γ_3	0.307[a]	1.08[c]
κ	−0.631[d]	3.09[d]
Optical matrix element (eV)		
E_p	19.6[a]	20.4[c]
Deformation potentials (eV)		
a_c	−2.08[e]	−2.78[e]
a_v	1.02[e]	1.22[e]
b	−4.7[e]	−0.7[e]
d	−8.14[f]	−1.21[f]
Mn *sp-d* exchange integrals (eV)		
$N_0\alpha$	0.22[g]	0.56[g]
$N_0\beta$	−1.8[g]	−2.37[g]
Young's modulus (kbar)		
E	461.42[h]	702.95[h]
Poisson's ratio		
ν	0.3746[h]	0.347[h]
Lattice constant (Å)		
a_0	5.81[i]	5.41[j]
Refractive index		
n_r	2.28[b]	2.27[b]

[a]From Ref. [66].
[b]From Ref. [67].
[c]From Ref. [68].
[d]From Eq. (A12).
[e]From Ref. [69].
[f]From Eq. (A19).
[g]From Ref. [70].
[h]From Ref. [71].
[i]From Ref. [72].
[j]From Ref. [73].

the Landau Hamiltonian, the Zeeman Hamiltonian, the strain Hamiltonian due to the lattice mismatch between the core and shell materials, and a Mn impurity Hamiltonian due to the *s-d* and *p-d* exchange interaction with localized Mn *d* electrons.

2. Landau Hamiltonian

The effective mass Hamiltonian in bulk narrow gap zinc-blende materials is given explicitly in Ref. [33]. To include the interaction with a magnetic field $\mathbf{B} = B\,\hat{\mathbf{z}}$ described by the vector potential $\mathbf{A}$, we use the standard Peierls substitution in which $\mathbf{p}$ in the bulk effective mass Hamiltonian is replaced by $\boldsymbol{\pi} = \mathbf{p} - e\mathbf{A}/c$ to obtain the Landau Hamiltonian [42,43,64]. The resulting Landau Hamiltonian is gauge invariant [64]. We use the symmetric gauge $\mathbf{A} = \frac{1}{2}\mathbf{B} \times \mathbf{r}$ so that the Cartesian components of the vector potential are $\mathbf{A} = \frac{B}{2}(-y,x,0)$.

It has been pointed out by Mlinar in the supplementary material of Ref. [65] that when numerically implementing the Peierls substitution, care must be taken so as not to destroy gauge invariance. Two tests are recommended to check for gauge invariance. The first test involves a change of gauge, say from the Landau to the symmetric gauge, while the second test involves changing the origin on the coordinate system. Both of these tests are beyond the scope of the present paper. Switching the origin of the quantum dot would substantially complicate the problem since we could no longer exploit the spherical symmetry of the dot. Many people have used the Peierls substitution and numerically solved the problem with a great deal of success [44–49].

Mlinar points out that one numerical problem with gauge invariance can arise from an incorrect discretization of the second derivative operator [65]. We believe that our numerical implementation is gauge invariant because (1) we use Dirichlet boundary conditions to preserve the phase of the wave functions and (2) we do not run into complications arising from discretization of derivative operators since we do not employ a numerical discretization scheme but instead expand the wave functions in a spherical box basis set as described below.

Since we are dealing with wide-gap materials, we ignore coupling between conduction and valence bands and arrive at the Landau Hamiltonian

$$H_L = \begin{bmatrix} L_a & L_c \\ L_c^\dagger & L_b \end{bmatrix} \tag{A4}$$

with the submatrices L_a, L_b, and L_c given by

$$L_a = \begin{bmatrix} E_g + A & 0 & 0 & 0 \\ 0 & -P - Q & -M & i\sqrt{2}M \\ 0 & -M^\dagger & -P + Q & i\sqrt{2}Q \\ 0 & -i\sqrt{2}M^\dagger & -i\sqrt{2}Q & -P - \Delta \end{bmatrix}, \tag{A5}$$

$$L_b = \begin{bmatrix} E_g + A & 0 & 0 & 0 \\ 0 & -P - Q & -M^\dagger & i\sqrt{2}M^\dagger \\ 0 & -M & -P + Q & i\sqrt{2}Q \\ 0 & -i\sqrt{2}M & -i\sqrt{2}Q & -P - \Delta \end{bmatrix}, \tag{A6}$$

$$L_c = \begin{bmatrix} 0 & 0 & 0 & 0 \\ 0 & 0 & -L & -i\sqrt{\frac{1}{2}}L \\ 0 & L & 0 & i\sqrt{\frac{3}{2}}L^\dagger \\ 0 & -i\sqrt{\frac{1}{2}}L & i\sqrt{\frac{3}{2}}L^\dagger & 0 \end{bmatrix}. \tag{A7}$$

In Eq. (A4), E_g is the band gap energy, and Δ is the spin-orbit splitting. The operators A, P, Q, L, and M are

$$A = \frac{1}{2m_0}(\pi_x\,\gamma_4\,\pi_x + \pi_y\,\gamma_4\,\pi_y + \pi_z\,\gamma_4\,\pi_z), \tag{A8a}$$

$$P = \frac{1}{2m_0}(\pi_x\,\gamma_1\,\pi_x + \pi_y\,\gamma_1\,\pi_y + \pi_z\,\gamma_1\,\pi_z), \tag{A8b}$$

$$Q = \frac{1}{2m_0}(\pi_x\ \gamma_2\ \pi_x + \pi_y\ \gamma_2\ \pi_y - 2\pi_z\ \gamma_2\ \pi_z), \tag{A8c}$$

$$L = -i\frac{\sqrt{3}}{m_0}\ \pi_{(-)}\ \gamma_3\ \pi_z, \tag{A8d}$$

and

$$M = \frac{\sqrt{3}}{2m_0}[\pi_{(-)}\ \gamma_{(+)}\ \pi_{(-)}\ -\ \pi_{(+)}\ \gamma_{(-)}\ \pi_{(+)}]. \tag{A8e}$$

The usual Luttinger parameters [42] are γ_1, γ_2, and γ_3 and we define $\gamma_4 = m_0/m_e^*$ as the inverse of the electron effective mass. We also define $\gamma_{(\pm)} = (\gamma_3 \pm \gamma_2)/2$ and $\pi_{(\pm)} = \pi_x \pm i\pi_y$. The operator ordering in Eq. (A8) matters when the material parameters are position dependent and ensures that the Hamiltonian matrix remains Hermitian. If we were to adopt the *axial approximation* and set $\gamma_2 = \gamma_3 = \overline{\gamma}$, we would have $\gamma_{(-)} = 0$ and the second term in Eq. (A8e) would vanish.

In the core-shell quantum dot we take $Q_c = 0.6$ for the conduction band offset between bulk CdS and ZnS. We take the zero of energy to be the top of the CdS valence band in which case H_L is given by Eq. (A4) without modification. For the ZnS shell the Landau Hamiltonian, H_L, is obtained by subtracting a constant energy from the diagonal operators in Eq. (A4) given by

$$E_0 = \Delta E_g(1 - Q_c), \tag{A9}$$

where $\Delta E_g = E_g(\text{ZnS}) - E_g(\text{CdS})$ is the band gap mismatch between the CdS core and ZnS shell.

3. Zeeman Hamiltonian

The Zeeman Hamiltonian is

$$H_Z = 2\,\mu_B\,B\begin{bmatrix} Z_a & 0 \\ 0 & -Z_a \end{bmatrix}, \tag{A10}$$

where $\mu_B = 5.789 \times 10^{-5}$ eV/T is the Bohr magneton and B is the applied magnetic field in teslas. The 4×4 submatrix Z_a is given by

$$Z_a = \begin{bmatrix} \frac{1}{2} & 0 & 0 & 0 \\ 0 & -\frac{3}{2}\kappa & 0 & 0 \\ 0 & 0 & \frac{1}{2}\kappa & -i\sqrt{\frac{1}{2}}(\kappa+1) \\ 0 & 0 & i\sqrt{\frac{1}{2}}(\kappa+1) & \kappa + \frac{1}{2} \end{bmatrix}. \tag{A11}$$

For the Luttinger parameter, κ, we use the approximation [42,63,74,75]

$$\kappa = \gamma_3 + \frac{2}{3}\,\gamma_2 - \frac{1}{3}\,\gamma_1 - \frac{2}{3}. \tag{A12}$$

By ignoring coupling between conduction and valence bands in the Zeeman Hamiltonian Eq. (A10), the effective electron gyromagnetic factor, g^*, describing the spin splitting between the electron spin-up and spin-down Landau levels at the band edge is $g^* = 2$. When coupling between conduction and valence bands is taken into account, a correction to g^* at the band edge can be obtained which is given by [61,76]

$$g^* = 2\left(1 - \frac{E_p}{2E_g}\frac{\Delta}{E_g + \Delta}\right). \tag{A13}$$

In the limit of large band gap energies, E_g, this expression reduces to $g^* = 2$ as expected. For the wide-gap semiconductors CdS and ZnS considered in this study, Eq. (A13) gives $g^* = 1.978$ and $g^* = 1.986$, respectively, using material parameters in Table I. Thus we are justified in using the estimate $g^* = 2$.

4. Strain Hamiltonian

Applying strain to a semiconductor alters the electronic band structure by deforming the unit cell. The effects on the electronic states due to strain-induced lattice deformation is described by the Bir-Pikus strain Hamiltonian [39]. The Bir-Pikus Hamiltonian is similar in structure to the Landau Hamiltonian and is given by

$$H_S = \begin{bmatrix} S_a & S_c \\ S_c^\dagger & S_b \end{bmatrix}, \tag{A14}$$

where the submatrices S_a, S_b, and S_c are

$$S_a = \begin{bmatrix} A_\varepsilon & 0 & 0 & 0 \\ 0 & -P_\varepsilon - Q_\varepsilon & -M_\varepsilon & i\sqrt{2}M_\varepsilon \\ 0 & -M_\varepsilon^\dagger & -P_\varepsilon + Q_\varepsilon & i\sqrt{2}Q_\varepsilon \\ 0 & -i\sqrt{2}M_\varepsilon^\dagger & -i\sqrt{2}Q_\varepsilon & -P_\varepsilon \end{bmatrix}, \tag{A15}$$

$$S_b = \begin{bmatrix} A_\varepsilon & 0 & 0 & 0 \\ 0 & -P_\varepsilon - Q_\varepsilon & -M_\varepsilon^\dagger & i\sqrt{2}M_\varepsilon^\dagger \\ 0 & -M_\varepsilon & -P_\varepsilon + Q_\varepsilon & i\sqrt{2}Q_\varepsilon \\ 0 & -i\sqrt{2}M_\varepsilon & -i\sqrt{2}Q_\varepsilon & -P_\varepsilon \end{bmatrix}, \tag{A16}$$

$$S_c = \begin{bmatrix} 0 & 0 & 0 & 0 \\ 0 & 0 & -L_\varepsilon & -i\sqrt{\frac{1}{2}}L_\varepsilon \\ 0 & L & 0 & i\sqrt{\frac{3}{2}}L_\varepsilon^\dagger \\ 0 & -i\sqrt{\frac{1}{2}}L_\varepsilon & i\sqrt{\frac{3}{2}}L_\varepsilon^\dagger & 0 \end{bmatrix}. \tag{A17}$$

The operators A_ε, P_ε, Q_ε, L_ε, and M_ε are related to the strain tensor components ε_{ij} and the deformation potentials a_c, a_v, b, and d by

$$A_\varepsilon = a_c(\varepsilon_{xx} + \varepsilon_{yy} + \varepsilon_{zz}), \tag{A18a}$$

$$P_\varepsilon = -a_v(\varepsilon_{xx} + \varepsilon_{yy} + \varepsilon_{zz}), \tag{A18b}$$

$$Q_\varepsilon = -\frac{b}{2}(\varepsilon_{xx} + \varepsilon_{yy} - 2\varepsilon_{zz}), \tag{A18c}$$

$$L_\varepsilon = id(\varepsilon_{xz} - i\varepsilon_{yz}), \tag{A18d}$$

and

$$M_\varepsilon = -\frac{b\sqrt{3}}{4}(\varepsilon_{xx} - \varepsilon_{yy}) + id\varepsilon_{xy}. \tag{A18e}$$

In Eq. (A18) we make the spherical approximation

$$d = \sqrt{3}\,b \tag{A19}$$

for simplicity.

The strain tensor components ε_{ij} are related to the displacement field $\mathbf{U}(\mathbf{r})$ by

$$\varepsilon_{ij} = \frac{1}{2}\left(\frac{\partial U_i}{\partial r_j} + \frac{\partial U_j}{\partial r_i}\right). \tag{A20}$$

The lattice constant mismatch between core and shell gives rise to a radial displacement field $\mathbf{U}(r) = U(r)\hat{\mathbf{r}}$. The calculation of the strain distribution in a spherical core-shell quantum dot is described in the Appendix of Ref. [57]. In modeling the mechanical properties of the spherical quantum dot, we assume the core and shell are homogenous and isotropic so the stress-strain relation is characterized by Young's modulus, E, and Poisson's ratio, ν. In the core region ($0 \leqslant r \leqslant R_c$) the radial displacement field, $U_c(r)$, is given by

$$U_c(r) = -r P_0 \frac{1-2\nu_c}{E_c}, \tag{A21}$$

where E_c and ν_c are Young's modulus and Poisson's ratio in the core and P_0 is the contact pressure at the core-shell interface at $r = R_c$. In the shell region ($R_c \leqslant r \leqslant R$) the radial displacement field, $U_s(r)$, in the limit of vanishing external applied pressure is

$$U_s(r) = r P_0 \frac{(1+\nu_s)}{E_s} \frac{\left[\frac{1-2\nu_s}{1+\nu_s} + \frac{1}{2}\left(\frac{R}{r}\right)^3\right]}{\left(\frac{R}{R_c}\right)^3 - 1}, \tag{A22}$$

where E_s and ν_s are Young's modulus and Poisson's ratio in the shell. The contact pressure P_0 is obtained from the shrink-fit boundary condition [57]

$$U_c(R_c) - U_s(R_c) = 2\left(\frac{a_{\text{shell}} - a_{\text{core}}}{a_{\text{shell}} + a_{\text{core}}}\right) R_c, \tag{A23}$$

where a_{core} and a_{shell} are the lattice constants in the core and shell regions.

5. Manganese impurity Hamiltonian

The exchange interaction between the Mn^{2+} d electrons and the conduction s and valence p electrons is treated in the virtual crystal and mean field approximation [40,41]. The resulting Mn sp-d exchange interaction Hamiltonian is [77]

$$H_{\text{Mn}} = x\, N_0 \langle S_z \rangle \begin{bmatrix} D_a & 0 \\ 0 & -D_a \end{bmatrix}, \tag{A24}$$

where x is the Mn concentration (mole fraction), N_0 is the number of unit cells per unit volume, and $\langle S_z \rangle$ is the average spin on a Mn site. The 4×4 submatrix D_a is

$$D_a = \begin{bmatrix} \frac{1}{2}\alpha & 0 & 0 & 0 \\ 0 & \frac{1}{2}\beta & 0 & 0 \\ 0 & 0 & -\frac{1}{6}\beta & -i\frac{\sqrt{2}}{3}\beta \\ 0 & 0 & i\frac{\sqrt{2}}{3}\beta & \frac{1}{6}\beta \end{bmatrix}, \tag{A25}$$

where $N_0\alpha$ and $N_0\beta$ are the s-d and p-d exchange integrals.

We assume by default that the core-shell nanoparticle is paramagnetic. In the paramagnetic phase, the average spin on a Mn site is given in the limit of noninteracting spins by

$$\langle S_z \rangle = -S\, B_S\left(gS\, \frac{\mu_B B}{kT}\right), \tag{A26}$$

where $g = 2$ and $S = \frac{5}{2}$ for the $3d^5$ electrons of the Mn^{++} ion [13]. The Brillouin function, $B_S(x)$, is defined as

$$B_S(x) = \frac{2S+1}{2S} \coth\left(\frac{2S+1}{2S}x\right) - \frac{1}{2S} \coth\left(\frac{x}{2S}\right). \tag{A27}$$

The antiparallel orientation of B and $\langle S_z \rangle$ is due to the difference in sign of the magnetic moment and the electron spin. Since B is directed along the z axis, the average Mn spin saturates at $\langle S_z \rangle = -\frac{5}{2}$.

If ferromagnetic core-shell nanoparticles exist they could be treated in the mean field approximation by taking the Curie temperature as an input parameter. In this case the average spin on a Mn site would be obtained by solving a transcendental equation for $\langle S_z \rangle$ as described in Ref. [78].

The Mn impurities are confined to an infinitely thin Mn doping shell at $r = R_i$ and we assume the Mn ions sit on Cd or Zn sites ($Cd_{1-x}Mn_xS$ or $Zn_{1-x}Mn_xS$) as they do in bulk samples [13]. If N_i is the number of Mn impurities in the Mn doping shell, the position-dependent Mn concentration, x, is given by

$$x(r) = \frac{N_i a_i^3}{16\pi R_i^2} \delta(r - R_i), \tag{A28}$$

where a_i is the lattice constant at $r = R_i$.

To compare our radial position doped nanoparticles with bulk samples, we define an effective bulk Mn concentration $\langle x \rangle$ by imagining the Mn impurities in the doping shell spread out uniformly inside the nanoparticle. If the N_i Mn impurities are uniformly distributed in a core-shell nanoparticle of radius R, the effective bulk Mn concentration is

$$\langle x \rangle = N_i \frac{3}{16\pi} \left(\frac{a}{R}\right)^3, \tag{A29}$$

where a is the volume-averaged nanoparticle lattice constant. For the core-shell nanoparticles considered in this paper, we take $a \approx 5.6$ Å and obtain the approximate expression

$$\langle x \rangle \approx 10.48 \frac{N_i}{R^3}, \tag{A30}$$

where R is in angstroms and the resulting $\langle x \rangle$ is dimensionless. For a 100 Å diameter core-shell nanoparticle radially position doped with 4 Mn impurities ($N_i = 4$), we find $\langle x \rangle \approx 3.3 \times 10^{-4}$. This is much smaller than the Mn doping in diluted magnetic semiconductor systems.

6. Electronic states and magneto-optical properties

The single-particle electronic state wave functions are given by the following expansion:

$$|\Psi\rangle = \sum_{\nu} \sum_{nlm} C^{\nu}_{nlm} |nlm\rangle\, |\nu\rangle, \tag{A31}$$

where C^{ν}_{nlm} are complex expansion coefficients and $|\nu\rangle$ are the eight Bloch basis states $\nu = 1 \ldots 8$ defined in Eqs. (A2) and (A3).

The summation indices n, l, and m satisfy $0 \leqslant n \leqslant N, 0 \leqslant l \leqslant n$, and $-l \leqslant m \leqslant l$. For a given N the number of n,l,m basis states is $N(N+1)(2N+1)/6$. For our simulations, we use $N = 6$. To verify that $N = 6$ is sufficient for convergence, we tried $N = 7$ which increases the number of n,l,m basis states from 91 to 140. For a 100 Å diameter core-shell nanoparticle with a 50 Å diameter CdS core, we found that increasing N from 6 to 7 shifted the ground state electron and hole energies at $B = 0$ by 0.8 meV and 0.56 meV, respectively.

The effective mass envelope basis functions in spherical polar coordinates (r,θ,ϕ) are given by the complete orthonormal set

$$|nlm\rangle = R_{nl}(r)\, Y_l^m(\theta,\phi). \tag{A32}$$

The angular envelope basis functions $Y_l^m(\theta,\phi)$ are the usual spherical harmonics. The radial envelope functions vanish at the surface of the quantum dot and are given by

$$R_{nl}(r) = \sqrt{\frac{2}{R^3}}\,\frac{1}{j_{l+1}\left(X_n^l\right)}\, j_l\left(X_n^l \frac{r}{R}\right), \tag{A33}$$

where $j_l(x)$ is the spherical Bessel function and X_n^l is the nth zero of $j_l(x)$.

The energies and expansion coefficients are obtained by solving the effective mass Schrödinger equation

$$\sum_{\nu'}\sum_{n'l'm'} \langle nlm|H_{\nu\nu'}|n'l'm'\rangle C^{\nu'}_{n'l'm'} = E\, C^{\nu}_{nlm}. \tag{A34}$$

The 8×8 Hamiltonian operators $H_{\nu\nu'}$ are the matrix elements in Eq. (A1). In evaluating the matrix elements in the Schrödinger equation (A34), we first convert the effective mass Hamiltonian operators in the Landau, Zeeman, strain, and manganese impurity Hamiltonians from Cartesian to spherical polar coordinates.

We calculate the magneto-optical absorption coefficient at the photon energy $\hbar\omega$ using the expression [79]

$$\alpha(\hbar\omega) = \frac{\hbar\omega}{(\hbar c)n_r}\epsilon_2(\hbar\omega), \tag{A35}$$

where $\epsilon_2(\hbar\omega)$ is the imaginary part of the dielectric function and n_r is the real part of the index of refraction.

In thermal equilibrium, the imaginary part of the dielectric function obtained from Fermi's golden rule is

$$\varepsilon_2(\hbar\omega) = \frac{4\pi^2 e^2}{V_0(\hbar\omega)^2}\sum_{IJ}|\hat{\varepsilon}\cdot P_{IJ}|^2 f_{JI}\delta(\Delta E_{IJ}-\hbar\omega). \tag{A36}$$

In the above equation, V_0 is the quantum dot volume, I and J label the quantum dot energy levels obtained from solving the effective mass Schrödinger equation, and the transition energies are $\Delta E_{IJ} = E_I - E_J$. In thermal equilibrium $f_{JI} = f_J - f_I$ where f_I, the probability that state I with energy E_I is occupied, is given by the Fermi-Dirac distribution function

$$f_I = \frac{1}{1+\exp[(E_I - E_f)/kT]}, \tag{A37}$$

where E_f is the Fermi level and kT is the thermal energy. The unit electric polarization vector is $\hat{\varepsilon}$ and P_{IJ} is the momentum matrix element between states I and J. Cartesian components of the 8×8 momentum operator P in our Bloch state basis are given in Appendix B of Ref. [61].

7. Magnetic g factors

We calculate electron and hole magnetic g factors numerically. From Eq. (2), we see that

$$g = \frac{1}{2|J_z|\mu_B}\frac{d}{dB}\left[E_\uparrow(B) - E_\downarrow(B)\right], \tag{A38}$$

where the derivative with respect to B is evaluated at $B=0$. In Eq. (A38), $|J_z|$ is the absolute value of the z component of the electron or hole angular momentum, μ_B is the Bohr magneton, and $E_|(B)$ and $E_|(B)$ are the spin-up and spin-down energies as functions of the magnetic field, respectively. The derivatives are evaluated numerically from the fan diagram defined on an evenly spaced grid using the second-order-accurate finite-difference formula [80]

$$\frac{d}{dx}f_0 \approx -\frac{3}{2h}f_0 + \frac{2}{h}f_1 - \frac{1}{2h}f_2 + o(h^2), \tag{A39}$$

where h is the grid spacing and $f_i \equiv f(i\,h)$.

As a consistency check on our calculations, we can estimate the effective electron g factor under the following assumptions: (1) Mn impurities are uniformly distributed in the CdS core, (2) electrons are completely confined in the core, and (3) changes in the effective g factor from the bulk value of 2 are primarily determined by the interaction of the electrons with the Mn impurity *sp-d* exchange Hamiltonian given in Eq. (A24). In this simple case, the effective electron g factor is given by

$$g = 2 + \frac{\langle S_z\rangle\langle x\rangle N_0\alpha}{\mu_B}, \tag{A40}$$

where the *s-d* exchange interaction $N_0\alpha = 0.22$ eV in the CdS core is taken from Table I and the effective Mn concentration is obtained from Eq. (A29) with $R = R_c$ taken to be the core radius. Expanding $\langle S_z\rangle$ in Eq. (A26) to lowest order in a Taylor series in powers of B, we obtain the low-field g factor

$$g = 2 - \frac{35N_i}{32\pi}\frac{N_0\alpha}{k_B T}\left(\frac{a}{R_c}\right)^3. \tag{A41}$$

Our analysis is analogous to the treatment of Mn-doping-dependent Zeeman splittings and effective g factors in Mn-doped CdS nanocrystals as described in Eq. (1) of Ref. [81].

This simple formula illustrates several qualitative results. First, the introduction of Mn impurities in the core acts to reduce the electron magnetic g factor from its bulk value of $g=2$. Second, the reduction in the electron g factor is directly proportional to the number of Mn impurities and is inversely proportional to the lattice temperature and the cube of the core radius.

[1] S. M. Sze and K. K. Ng, *Physics of Semiconductor Devices* (John Wiley & Sons, 2006).

[2] S. L. Chuang, *Physics of Optoelectronic Devices* (Wiley, New York, 1995).

[3] D. D. Awschalom and M. E. Flatté, Nat. Phys. **3**, 153 (2007).

[4] S. Wolf, D. Awschalom, R. Buhrman, J. Daughton, S. Von Molnar, M. Roukes, A. Y. Chtchelkanova, and D. Treger, Science **294**, 1488 (2001).

[5] D. D. Awschalom, M. E. Flatté, and N. Samarth, Sci. Am. **286**, 66 (2002).

[6] Y. Ohno, D. Young, B. Beschoten, F. Matsukura, H. Ohno, and D. Awschalom, Nature (London) **402**, 790 (1999).

[7] H. Munekata, T. Abe, S. Koshihara, A. Oiwa, M. Hirasawa, S. Katsumoto, Y. Iye, C. Urano, and H. Takagi, J. Appl. Phys. **81**, 4862 (1997).

[8] S. Koshihara, A. Oiwa, M. Hirasawa, S. Katsumoto, Y. Iye, C. Urano, H. Takagi, and H. Munekata, Phys. Rev. Lett. **78**, 4617 (1997).

[9] T. Dietl, Nat. Mater. **9**, 965 (2010).

[10] T. Dietl and H. Ohno, Rev. Mod. Phys. **86**, 187 (2014).

[11] K. Sato, L. Bergqvist, J. Kudrnovský, P. H. Dederichs, O. Eriksson, I. Turek, B. Sanyal, G. Bouzerar, H. Katayama-Yoshida, V. A. Dinh *et al.*, Rev. Mod. Phys. **82**, 1633 (2010).

[12] T. Jungwirth, J. Sinova, J. Mašek, J. Kučera, and A. H. MacDonald, Rev. Mod. Phys. **78**, 809 (2006).

[13] J. K. Furdyna, J. Appl. Phys. **64**, R29 (1988).

[14] M. A. Meeker, B. A. Magill, G. A. Khodaparast, D. Saha, C. J. Stanton, S. McGill, and B. W. Wessels, Phys. Rev. B **92**, 125203 (2015).

[15] R. G. Chaudhuri and S. Paria, Chem. Rev. **112**, 2373 (2011).

[16] J. van Embden, J. Jasieniak, D. E. Gómez, P. Mulvaney, and M. Giersig, Aust. J. Chem. **60**, 457 (2007).

[17] Y. Cao and U. Banin, J. Am. Chem. Soc. **122**, 9692 (2000).

[18] J. J. Li, Y. A. Wang, W. Guo, J. C. Keay, T. D. Mishima, M. B. Johnson, and X. Peng, J. Am. Chem. Soc. **125**, 12567 (2003).

[19] Y. Lei and W.-K. Chim, J. Am. Chem. Soc. **127**, 1487 (2005).

[20] Y. Yang, O. Chen, A. Angerhofer, and Y. C. Cao, J. Am. Chem. Soc. **128**, 12428 (2006).

[21] A. R. Loukanov, C. D. Dushkin, K. I. Papazova, A. V. Kirov, M. V. Abrashev, and E. Adachi, Colloids Surf. A **245**, 9 (2004).

[22] Y. Yang, O. Chen, A. Angerhofer, and Y. C. Cao, J. Am. Chem. Soc. **130**, 1564 (2008).

[23] Y. Yang, O. Chen, A. Angerhofer, and Y. C. Cao, Chem. Eur. J. **15**, 3186 (2009).

[24] O. Chen, D. E. Shelby, Y. Yang, J. Zhuang, T. Wang, C. Niu, N. Omenetto, and Y. C. Cao, Angew. Chem. **122**, 10330 (2010).

[25] S. Ithurria, P. Guyot-Sionnest, B. Mahler, and B. Dubertret, Phys. Rev. Lett. **99**, 265501 (2007).

[26] P. De Farias, B. Santos, F. Menezes, A. Brasil Jr., R. Ferreira, M. Motta, A. Castro-Neto, A. Vieira, D. Silva, A. Fontes *et al.*, Appl. Phys. A **89**, 957 (2007).

[27] P. Reiss, M. Protiere, and L. Li, Small **5**, 154 (2009).

[28] D. J. Norris, A. L. Efros, and S. C. Erwin, Science **319**, 1776 (2008).

[29] R. Thakar, Y. Chen, and P. T. Snee, Nano Lett. **7**, 3429 (2007).

[30] A. Makhal, H. Yan, P. Lemmens, and S. K. Pal, J. Phys. Chem. C **114**, 627 (2009).

[31] D. Sun, Y. Tian, Y. Zhang, Z. Xu, M. Y. Sfeir, M. Cotlet, and O. Gang, ACS Nano **9**, 5657 (2015).

[32] S. Fillipov, Y. Puttisong, Y. Huang, I. A. Buyanova, S. Suraprapapich, C. W. Tu, and W. M. Chen, ACS Nano **9**, 5741 (2015).

[33] A. L. Efros and M. Rosen, Phys. Rev. B **58**, 7120 (1998).

[34] J.-B. Xia and J. Li, Phys. Rev. B **60**, 11540 (1999).

[35] D. Schooss, A. Mews, A. Eychmüller, and H. Weller, Phys. Rev. B **49**, 17072 (1994).

[36] O. I. Micic, B. B. Smith, and A. J. Nozik, J. Phys. Chem. B **104**, 12149 (2000).

[37] A. C. Bartnik, F. W. Wise, A. Kigel, and E. Lifshitz, Phys. Rev. B **75**, 245424 (2007).

[38] A. Kalameitsev and A. V. Chaplik, JETP Lett. **100**, 177 (2014).

[39] G. L. Bir and G. E. Pikus, *Symmetry and Strain-Induced Effects in Semiconductors* (Wiley, New York, 1974).

[40] R. J. Nicholas, M. J. Lawless, H. H. Cheng, D. E. Ashenford, and B. Lunn, Semicond. Sci. Technol. **10**, 791 (1995).

[41] J. Gaj, R. Planel, and G. Fishman, Solid State Commun. **29**, 435 (1979).

[42] J. M. Luttinger, Phys. Rev. **102**, 1030 (1956).

[43] V. Mlinar, M. Tadić, B. Partoens, and F. Peeters, Phys. Rev. B **71**, 205305 (2005).

[44] H. Chu and Y.-C. Chang, Phys. Rev. B **40**, 5497 (1989).

[45] F. B. Pedersen and Y.-C. Chang, Phys. Rev. B **55**, 4580 (1997).

[46] V. Mlinar, A. Schliwa, D. Bimberg, and F. Peeters, Phys. Rev. B **75**, 205308 (2007).

[47] A. Cresti, Nanotechnology **18**, 055403 (2007).

[48] E. Tsitsishvili, G. S. Lozano, and A. O. Gogolin, Phys. Rev. B **70**, 115316 (2004).

[49] H. Xu, T. Heinzel, and I. Zozoulenko, Phys. Rev. B **84**, 035319 (2011).

[50] L. Brus, J. Phys. Chem. **90**, 2555 (1986).

[51] Y. Wang, A. Suna, W. Mahler, and R. Kasowski, J. Chem. Phys. **87**, 7315 (1987).

[52] P. E. Lippens and M. Lannoo, Phys. Rev. B **39**, 10935 (1989).

[53] Y. Wang and N. Herron, Phys. Rev. B **42**, 7253 (1990).

[54] T. Rajh, O. I. Micic, and A. J. Nozik, J. Phys. Chem. **97**, 11999 (1993).

[55] A. S. Baimuratov, I. D. Rukhlenko, V. K. Turkov, I. O. Ponomareva, M. Y. Leonov, T. S. Perova, K. Berwick, A. V. Baranov, and A. V. Fedorov, Sci. Rep. **4**, 6917 (2014).

[56] R. B. Little, M. A. El-Sayed, G. W. Bryant, and S. Burke, J. Chem. Phys. **114**, 1813 (2001).

[57] J. Rockenberger, L. Tröger, A. L. Rogach, M. Tischer, M. Grundmann, A. Eychmüller, and H. Weller, J. Chem. Phys. **108**, 7807 (1998).

[58] A. Yamagishi and M. Date, Physica B (Amsterdam, Neth.) **155**, 91 (1989).

[59] J. Singleton, C. Mielke, A. Migliori, G. Boebinger, and A. Lacerda, Physica B (Amsterdam, Neth.) **346**, 614 (2004).

[60] J. Wosnitza, A. Bianchi, J. Freudenberger, J. Haase, T. Herrmannsdörfer, N. Kozlova, L. Schultz, Y. Skourski, S. Zherlitsyn, and S. Zvyagin, J. Magn. Magn. Mater. **310**, 2728 (2007).

[61] G. D. Sanders, Y. Sun, F. V. Kyrychenko, C. J. Stanton, G. A. Khodaparast, M. A. Zudov, J. Kono, Y. H. Matsuda, N. Miura, and H. Munekata, Phys. Rev. B **68**, 165205 (2003).

[62] A. Pandey, S. Brovelli, R. Viswanatha, L. Li, J. Pietryga, V. Klimov, and S. Crooker, Nat. Nanotechnol. **7**, 792 (2012).

[63] C. R. Pidgeon and R. N. Brown, Phys. Rev. **146**, 575 (1966).

[64] J. M. Luttinger, Phys. Rev. **84**, 814 (1951).

[65] V. Mlinar, J. Mater. Chem. **22**, 1724 (2012).

[66] W. Jaskólski and G. W. Bryant, Phys. Rev. B **57**, R4237 (1998).

[67] P. Hervè and L. K. J. Vandamme, Infrared Phys. Technol. **35**, 609 (1994).

[68] P. Lawaetz, Phys. Rev. B **4**, 3460 (1971).

[69] T. Taguchi, C. Onodera, Y. Yamada, and Y. Masumoto, Jpn. J. Appl. Phys. **32**, L1308 (1993).

[70] R. Beaulac and D. R. Gamelin, Phys. Rev. B **82**, 224401 (2010).
[71] B. Thomas and M. Abdulkhadar, Solid State Commun. **94**, 205 (1995).
[72] G. T. Einevoll, Phys. Rev. B **45**, 3410 (1992).
[73] P. Wright and B. Cockayne, J. Cryst. Growth **59**, 148 (1982).
[74] G. Dresselhaus, A. F. Kip, and C. Kittel, Phys. Rev. **98**, 368 (1955).
[75] G. Dresselhaus, Phys. Rev. **100**, 580 (1955).
[76] C. Rigaux, Semiconductors and Semimetals **25**, 229 (1988).
[77] J. Kossut, Semiconductors and Semimetals **25**, 183 (1988).
[78] M. Bhowmick, T. R. Merritt, G. A. Khodaparast, B. W. Wessels, S. A. McGill, D. Saha, X. Pan, G. D. Sanders, and C. J. Stanton, Phys. Rev. B **85**, 125313 (2012).
[79] F. Bassani and G. P. Parravicini, *Electronic States and Optical Transitions in Solids* (Pergamon, New York, 1975).
[80] B. Fornberg, Math. Comput. **51**, 699 (1988).
[81] S. Taguchi, A. Ishizumi, T. Tayagaki, and Y. Kanemitsu, Appl. Phys. Lett. **94**, 173101 (2009).